DRAFT VERSION OCTOBER 24, 2018
Preprint typeset using LaTeX style emulateapj v. 01/23/15

PARABOLIC JETS FROM THE SPINNING BLACK HOLE IN M87

MASANORI NAKAMURA[1], KEIICHI ASADA[1], KAZUHIRO HADA[2], HUNG-YI PU[3,1], SCOTT NOBLE[4,5], CHIHYIN TSENG[6,1], KENJI TOMA[7], MOTOKI KINO[8,9], HIROSHI NAGAI[9], KAZUYA TAKAHASHI[10] JUAN-CARLOS ALGABA[11], MONICA ORIENTI[12], KAZUNORI AKIYAMA[13,14,2], AKIHIRO DOI[15], GABRIELE GIOVANNINI[16,12], MARCELLO GIROLETTI[12], MAREKI HONMA[2], SHOKO KOYAMA[1], ROCCO LICO[17,16,12], KOTARO NIINUMA[18], FUMIE TAZAKI[2]

[1]Institute of Astronomy & Astrophysics, Academia Sinica, 11F of Astronomy-Mathematics Building, AS/NTU No. 1, Taipei 10617, Taiwan
[2]Mizusawa VLBI Observatory, National Astronomical Observatory of Japan, Osawa, Mitaka, Tokyo 181-8588, Japan
[3]Perimeter Institute for Theoretical Physics, 31 Caroline Street North, Waterloo, ON, N2L 2Y5, Canada
[4]Department of Physics and Engineering Physics, University of Tulsa, Tulsa, OK 74104, USA
[5]Gravitational Astrophysics Laboratory, NASA Goddard Space Flight Center, Greenbelt, MD 20771, USA
[6]Department of Physics, National Taiwan University, Taipei 10617, Taiwan
[7]Astronomical Institute, Tohoku University, Sendai 980-8578, Japan
[8]Kogakuin University, Academic Support Center, 2665-1 Nakano, Hachioji, Tokyo 192-0015, Japan
[9]National Astronomical Observatory of Japan, Osawa, Mitaka, Tokyo 181-8588, Japan
[10]Yukawa Institute for Theoretical Physics, Kyoto University, Kyoto, 606-8502, Japan
[11]Department of Physics and Astronomy, Seoul National University, 1 Gwanak-ro, Gwanak-gu, Seoul 08826, Korea
[12]INAF-Istituto di Radio Astronomia, via P. Gobetti 101, I-40129 Bologna, Italy
[13]National Radio Astronomy Observatory, 520 Edgemont Rd, Charlottesville, VA, 22903, USA
[14]Massachusetts Institute of Technology, Haystack Observatory, 99 Millstone Road, Westford, MA 01886, USA
[15]Institute of Space and Astronautical Science, Japan Aerospace Exploration Agency, 3-1-1 Yoshinodai, Chuou-ku, Sagamihara, 252-5210, Kanagawa, Japan
[16]Dipartimento di Fisica e Astronomia, Universita di Bologna, via Gobetti 93/2, 40129 Bologna, Italy
[17]Max-Planck-Institut für Radioastronomie, Auf dem Hügel 69, D-53121 Bonn, Germany and
[18]Graduate School of Science and Engineering, Yamaguchi University, 753-8511, Yamaguchi, Japan
nakamura@asiaa.sinica.edu.tw

Draft version October 24, 2018

ABSTRACT

The M87 jet is extensively examined by utilizing general relativistic magnetohydrodynamic (GRMHD) simulations as well as the steady axisymmetric force-free electrodynamic (FFE) solution. Quasi-steady funnel jets are obtained in GRMHD simulations up to the scale of ~ 100 gravitational radius ($r_{\rm g}$) for various black hole (BH) spins. As is known, the funnel edge is approximately determined by the following equipartitions; i) the magnetic and rest-mass energy densities and ii) the gas and magnetic pressures. Our numerical results give an additional factor that they follow the outermost parabolic streamline of the FFE solution, which is anchored to the event horizon on the equatorial plane. We also identify the matter dominated, non-relativistic corona/wind play a dynamical role in shaping the funnel jet into the parabolic geometry. We confirm a quantitative overlap between the outermost parabolic streamline of the FFE jet and the edge of jet sheath in VLBI observations at $\sim 10^1$–$10^5\,r_{\rm g}$, suggesting that the M87 jet is likely powered by the spinning BH. Our GRMHD simulations also indicate a lateral stratification of the bulk acceleration (i.e., the spine-sheath structure) as well as an emergence of knotty superluminal features. The spin characterizes the location of the jet stagnation surface inside the funnel. We suggest that the limb-brightened feature could be associated with the nature of the BH-driven jet, if the Doppler beaming is a dominant factor. Our findings can be examined with (sub-)mm VLBI observations, giving a clue for the origin of the M87 jet.

Subject headings: galaxies: active — galaxies: individual (M 87) — galaxies:jets — magnetohydrodynamics (MHD) — methods: data analysis — methods: analytical

1. INTRODUCTION

Active galactic nuclei (AGN) jets are widely believed to be initiated in the vicinity of supermassive black holes (SMBHs)—with masses $M \simeq 10^7$–$10^{10}\,M_\odot$—at around the gravitational radius $r_{\rm g}$ ($\lesssim$ milliparsec) and extend up to a scale of $\sim$ megaparsec (Mpc) as giant radio lobes. Force-free electrodynamic (FFE) and/or magnetohydrodynamic (MHD) mechanisms are frequently invoked to extract energy and momentum from a star, compact object, or an accretion disk around either (e.g. Blandford & Znajek 1977; Blandford & Payne 1982; Uchida & Shibata 1985; Lovelace et al. 1987; Meier et al. 2001; Beskin 2010; Meier 2012). Key issues to be answered are the mechanism for bulk acceleration up to the relativistic regime as is inferred from the superluminal motions $\lesssim 40\,c$ (the speed of light) and high brightness temperatures observed (Lister et al. 2013), as well as the huge amount of energy $\lesssim 10^{60}$–10^{61} erg deposited into the intracluster medium in the magnetic (e.g. Kronberg et al. 2001) and/or kinetic (e.g. Ghisellini et al. 2014) forms during their duty cycles of $\sim 10^7$–10^8 years. The power of relativistic jets may be larger than the accretion luminosity, implying that a rotating black hole may play a role (Ghisellini et al. 2014).

Special or general relativistic MHD (SRMHD or GRMHD) flows with a generalized parabolic geometry [where $z \propto R^\epsilon$ in the cylindrical coordinates (R, z) with $\epsilon > 1$] could be accelerated due to the so-called "magnetic nozzle effect"[1] (Camenzind 1987; Li et al. 1992; Begelman & Li 1994) in the

[1] An effective separation between neighboring poloidal field lines (faster than rate at which their cross-sectional radius increases) causes an efficient conversion from the Poynting to matter energy flux along a streamline.

trans-to-super fast magnetosonic regime. The Lorentz factor $\Gamma \gtrsim 10$ is confirmed at large distances of $z/r_{\rm g} \gtrsim 10^3$ by utilizing semi-analytical steady solutions and numerical simulations (e.g. Li et al. 1992; Begelman & Li 1994; Contopoulos 1995; Vlahakis & Königl 2003a,b; Tomimatsu & Takahashi 2003; Fendt & Ouyed 2004; Beskin & Nokhrina 2006, 2009; Komissarov et al. 2007, 2009; Tchekhovskoy et al. 2009; Lyubarsky 2009, 2010; Toma & Takahara 2013). An even higher Γ is obtained in semi-analytical/numerical studies of FFE jets (Narayan et al. 2007; Tchekhovskoy et al. 2008)[2].

The value Γ of a cold, relativistic MHD (Poynting flux-dominated: PFD) outflow is related to μ, the total [matter (kinetic plus rest-mass) + electromagnetic] energy flux per unit rest-mass energy flux (e.g. Toma & Takahara 2013):

$$\mu/\Gamma = 1 + \sigma, \tag{1}$$

where σ is the Poynting flux per unit matter energy flux (i.e., so-called "magnetization"), and μ is constant along a streamline (poloidal magnetic field line) in a steady axisymmetric ideal-MHD flow. Therefore, Γ approaches its maximum value $\Gamma_\infty \simeq \mu$ with $\sigma_\infty \simeq 0$, when a full conversion of electromagnetic energy to matter kinetic energy occurs. It is, however, still unknown how/where the MHD bulk acceleration is terminated in the realistic galactic environment, or what value is σ_∞. Also, the radial (R) expansion of MHD jets naturally produces a lateral stratification of Γ in the jet interior with a different evolution of ϵ and σ (McKinney 2006; Komissarov et al. 2007, 2009; Tchekhovskoy et al. 2009). Recently, values of $\mu \lesssim 30$ are suggested, which implies $\sigma_\infty \lesssim 1$, although $\mu \sim$ 10-10^3 could be expected in the MHD regime for relativistic outflows (Nokhrina et al. 2015).

M87 is one of the nearest active radio galaxies (16.7 Mpc; Blakeslee et al. 2009) that exhibits subliminal to superluminal motions (see, Figure 16 and references therein). With its proximity, the black hole mass M is estimated to be in a range of $(3.3-6.2)\times10^9 M_\odot$ (e.g. Macchetto et al. 1997; Gebhardt & Thomas 2009; Gebhardt et al. 2011; Walsh et al. 2013). The largest mass of $6.2\times10^9 M_\odot$ gives an apparent angular size $\sim 3.7\,\mu{\rm as}/r_{\rm g}$. This galaxy therefore provides a unique opportunity to study a relativistic outflow with the highest angular resolution in units of $r_{\rm g}$. Global mm VLBI observations, known as the Event Horizon Telescope (EHT) project, is expected to resolve the black hole shadow in M87 (Doeleman et al. 2012). Therefore, we also expect to resolve the jet launching region in the coming years.

Extended synchrotron emission of the one-sided jet, emerging from the nucleus, has been the target of multi-wavelength studies, from radio (see, Figure 15 and references therein) to X-ray bands for decades, which cover the scale of ~ 0.2 mas – 14 arcsec with the viewing angle $\theta_{\rm v} = 14^\circ$ (Wang & Zhou 2009), corresponding to $\sim 2.3\times10^2\,r_{\rm g}$ – $1.6\times10^7\,r_{\rm g}$ in de-projection. VLBI cores are considered to be the innermost jet emission at observed frequencies (Blandford & Königl 1979). Observations at cm to mm wavelengths (Hada et al. 2011) therefore may be used to explore the jet further upstream $\lesssim 200\,r_{\rm g}$ (Hada et al. 2013; Nakamura & Asada 2013) including the VLBI cores at 230 GHz by EHT observations (Doeleman et al. 2012; Akiyama et al. 2015). Examinations of VLBI cores in M87 suggest a strongly magnetized jet in the vicinity of the SMBH (Kino et al. 2015), challenging the classical equipartition paradigm.

From low to high frequency VLBI observations, "limb-brightened" features (dominated by the "jet sheath" emission) are widely confirmed on the scale $\sim$ 200–$10^5\,r_{\rm g}$ (in de-projection). Despite the fact various models are proposed for AGN jets in general (see, discussions by Kovalev et al. 2007), readers can refer specific models to the M87 jet on large scales $\gtrsim 10^3\,r_{\rm g}$; either a concentration of the magnetic flux at the outer boundary of the relativistic jet, which is confined by non-relativistic disk wind (Gracia et al. 2009), or a pileup of the material along the edge of the jet under the pressure equilibrium in the lateral direction (Zakamska et al. 2008). These models nicely reproduce the synthetic synchrotron map on pc scales ($\sim 10^3$–$10^4\,r_{\rm g}$), but both models suggest a relatively high $\Gamma \sim$ 10–15 on this spatial scale. Furthermore, the recent discovery of the "ridge-brightened" features (dominated by the "jet spine" emission) (Asada et al. 2016; Hada 2017) sheds light on the complex structure in the M87 jet at $\gtrsim$ mas ($\sim 10^3\,r_{\rm g}$) scales. This may be a direct confirmation of the jet "spine-sheath" structure in AGNs, but the emission mechanism there is not understood sufficiently well to provide a robust prediction of the "ridge+limb-brightened" feature.

One of the feasible ways to estimate the jet's global structure is to measure the Full Width Half Maximum (FWHM) of the transverse intensity as a diameter[3] at different frequencies and plot its radius (FWHM/2) as a function of the jet's axial distance (de-projected) in units of $r_{\rm g}$. This gives a proper sense how/where the jet streamline could be and where it originates in the vicinity of the SMBH. A linear fit on the log-log plot is very useful to investigate the jet structure in two-dimensional space (Asada & Nakamura 2012; Nakamura & Asada 2013; Hada et al. 2013). There are several preceding studies on the M87 jet (e.g. Broderick & Loeb 2009; Dexter et al. 2012; Mościbrodzka et al. 2016a) that investigate the horizon scale structure, but it is essential to conduct a direct comparison of the jet global structure in observations with theory and numerical simulations.

An accreting black hole plays a dynamically important role in producing relativistic jets, which has been demonstrated in GRMHD simulations during the past decade; a radiatively inefficient accretion flow (RIAF) with a poloidal magnetic flux and a spinning black hole are key ingredients for producing PFD funnel jets (e.g. Gammie et al. 2003; De Villiers et al. 2003, 2005; Hirose et al. 2004; McKinney & Gammie 2004; Hawley & Krolik 2006; McKinney 2006; Beckwith et al. 2008). The system can be directly applicable to low-luminosity AGNs (LLAGNs) such as M87. It has been examined that the M87 jet (sheath) is slowly collimated from a full opening angle of $\sim 60^\circ$ near the black hole to $\sim 10^\circ$ at large distances ($\gtrsim$ 10 pc; Junor et al. 1999). We note that the opening angle in Junor et al. (1999) is an *apparent* value in the sky projection. McKinney (2006) suggests that this wider sheath emission could be due to a RIAF wind (outside of a well-collimated relativistic cold PFD jet).

Regarding a co-existence of the PFD funnel jet and coronal wind from the RIAF, De Villiers et al. (2003, 2005) observed there to be a region of unbound mass flux at the boundary between the evacuated funnel and the coronal wind, referred to as the "funnel-wall" jet. The driving force could be

[2] An infinitely magnetized (i.e., force-free) fluid could have the same speed as the drift speed $V_{\rm d}$ of the electromagnetic ($\boldsymbol{E}$ and $\boldsymbol{B}$) fields; $V_{\rm d}/c = |\boldsymbol{E}\times\boldsymbol{B}|/B^2 = E/B$ ($\boldsymbol{E}\cdot\boldsymbol{B}$=0) and thus the Lorentz factor from the drift speed is $\Gamma^2 \approx 1/(1-V_{\rm d}^2/c^2) = B^2/(B^2-E^2)$.

[3] To evaluate the jet's width with a limb-brightened feature, two Gaussians are fitted to the slice profile of the jet and one can measure the separation between outer sides of the Half-maximum point of each Gaussian.

a high-pressure (gas + magnetic) corona squeezing material against an inner centrifugal wall, implying that the magneto-centrifugal mechanism (Blandford & Payne 1982, hereafter BP82) does play a minor role. Hawley & Krolik (2006) concluded that the precise shape and collimation of the entire outflow (PFD jet + funnel-wall jet + coronal wind) are uncertain for two reasons: i) the outer boundary of the matter-dominated funnel-wall jet is somewhat indistinct and ii) there is a smooth transition as a function of polar angle between mildly relativistic unbound matter and slightly slower but bound coronal matter. On the other hand, the boundary between the low-density PFD funnel jet interior and the high-density funnel-wall jet is sharp and clear. Properties of the coronal wind are investigated in GRMHD simulation with various black hole spins and different magnetic configurations (e.g. Narayan et al. 2012; Sadowski et al. 2013; Yuan et al. 2015), but there is no unique way to discriminate the boundary (Sadowski et al. 2013).

Comparisons of GRMHD simulations with steady solutions of the axisymmetric force-free disk wind (McKinney & Narayan 2007a) provide a fundamental similarity of the PFD funnel jet. In the fiducial GRMHD simulation, the vertically (height) integrated toroidal current, which is enclosed inside a radius, follows a remarkably similar power-law profile with the parabolic (or simply we use parabolic throughout this paper) solution ($\epsilon = 1.6$) of the disk wind (BP82), whereas the split-monopole ($\epsilon = 1$) or genuine paraboloidal ($\epsilon = 2$) solutions are well-known (Blandford & Znajek 1977, hereafter BZ77). This scaling is found to be maintained in a time-averaged sense, but also at each instant of time. It is also independent of the black hole spin. As a consequence, the poloidal magnetic field of the PFD jet in the GRMHD simulation agrees well with the force-free solution of a non-rotating thin disk having the parabolic geometry. McKinney & Narayan (2007b) performed general relativistic FFE (GRFFE) simulations of the disk wind. The magnetosphere of their GRFFE simulation with parabolic geometry also matches remarkably well to the PFD funnel jet in the fiducial GRMHD simulation, but no better than with the non-rotating force-free thin disk solution with the BP82-type parabolic geometry. It suggests that a rotation of the magnetic field leads to negligible "self-collimation".

Notable agreement of the BP82-type parabolic shape of the PFD funnel jet between GRMHD simulations and force-free (steady/time-dependent and/or non-rotating/rotating) models indicates that gas plus magnetic pressure of the wind/corona in GRMHD simulations is similar to the magnetic pressure in the FFE disk wind outside the funnel region. Note that McKinney & Narayan (2007b) considered only the portion of i) the steady solution of the axisymmetric FFE disk wind and ii) the GRFFE simulation of the disk wind (both winds are in the parabolic shape) that overlap the funnel jet region in the GRMHD simulation. So far, the boundary condition and the shape of the funnel edge are poorly constrained. It is also unclear where the footpoint of the outermost streamline of the PFD funnel jet will be anchored in the quasi-steady states of GRMHD simulations.

The collimation of the PFD funnel jet is still the issue. GRMHD simulations in the literature exhibit jet collimation ceasing at $\sim 50\, r_{\rm g}$ (Hawley & Krolik 2006). The largest simulations to date extend up to $r = 10^4\, r_{\rm g}$ (McKinney 2006) and show $\Gamma_\infty \lesssim 10$ saturated beyond $\sim$ a few of 100 $r_{\rm g}$ (despite $b^2/\rho \gg 1$), where the jet collimation terminates, following a conical expansion downstream. Global SRMHD or (GR)FFE simulations with a "fixed" curvilinear boundary wall (i.e., parabolic; Komissarov et al. 2007, 2009; Tchekhovskoy et al. 2008, 2010) show bulk acceleration up to $\Gamma_\infty \sim 10^1$–10^3, whereas it is still unclear how such a highly relativistic flow can be stably confined in a realistic environment. A recent semi-analytical model shows that the collimation of PFD jets may take place by the wind in RIAFs, if the total wind power $P_{\rm wind}$ exceeds about 10% of the jet power $P_{\rm jet}$ (Globus & Levinson 2016), while $P_{\rm wind}/\dot{M}c^2 \approx 10^{-3}$ (where $\dot{M}$ denotes the mass accretion rate at the horizon) is obtained by a GRMHD simulation around the Schwarzschild black hole (Yuan et al. 2015).

In this paper, we examine the structure of the PFD funnel jet with GRMHD simulations. The funnel edge is compared with steady self-similar solutions of the axisymmetric FFE jet and we derive the physical conditions of the boundary between the funnel jet and outside (wind/corona). Results are compared with the M87 jet sheath in VLBI observations. Methods and results for examining a parabolic jet streamline are presented in Sections 2 and 3. Comparison with VLBI observations is given in Section 4. Based on our results, Section 5 assigns topical discussions and prospects for exploring the origin of the M87 jet with mm/sub-mm VLBI observations in the near future. Conclusions are provided in Section 6.

2. METHODS

We conduct a direct comparison between the observed jet geometry in M87 and theoretical/numerical models. The present paper investigates especially the part of parabolic streams inside the SMBH's sphere of influence. Quasi-steady black hole ergosphere-driven jets are self-consistently generated from GRMHD simulations, and their connection to mm/cm VLBI images is examined by utilizing steady axisymmetric FFE jet solutions.

2.1. *Funnel Jet Boundary in the FFE Approximation*

According to a steady self-similar solution of the axisymmetric FFE jet (Narayan et al. 2007; Tchekhovskoy et al. 2008, hereafter NMF07, TMN08), we consider here an approximate formula of the magnetic stream function $\Psi(r,\theta)$ in polar (r,θ) coordinates in the Boyer-Lindquist frame (Tchekhovskoy et al. 2010):

$$\Psi(r,\theta) = \left(\frac{r}{r_{\rm H}}\right)^{\kappa} (1-\cos\theta), \tag{2}$$

where $r_{\rm H} = r_{\rm g}(1+\sqrt{1-a^2})$ is the radius of the black hole horizon, and the dimensionless Kerr parameter $a = J/J_{\rm max}$ describes the black hole spin. J is the black hole angular momentum and its maximum value is given by $J_{\rm max} = r_{\rm g}Mc = GM^2/c$, where G is the gravitational constant. $0 \le \kappa \le 1.25$ and $0 \le \theta \le \pi/2$ are adopted in TMN08. Ψ is conserved along each field (stream-) line in a steady solution of the axisymmetric MHD outflow[4]. If $\kappa = 0$ is chosen, the asymptotic streamline has a split-monopole (radial) shape $z \propto R$ (where, $R = r\sin\theta$ and $z = r\cos\theta$), whereas if $\kappa = 1$ is chosen, the streamline has the (genuine) parabolic shape $z \propto R^2$ at $R \gg r_{\rm g}$ (BZ77). $\kappa = 0.75$ is the case of the parabolic shape $z \propto R^{1.6}$ (BP82), which is important in this paper.

[4] An asymptotic flow ($r/r_{\rm H} \gg 1$) follows $z \propto R^{\epsilon}$, where $\epsilon = 2/(2-\kappa)$, which includes conical and parabolic shapes ($1 \le \epsilon \le 2.67$).

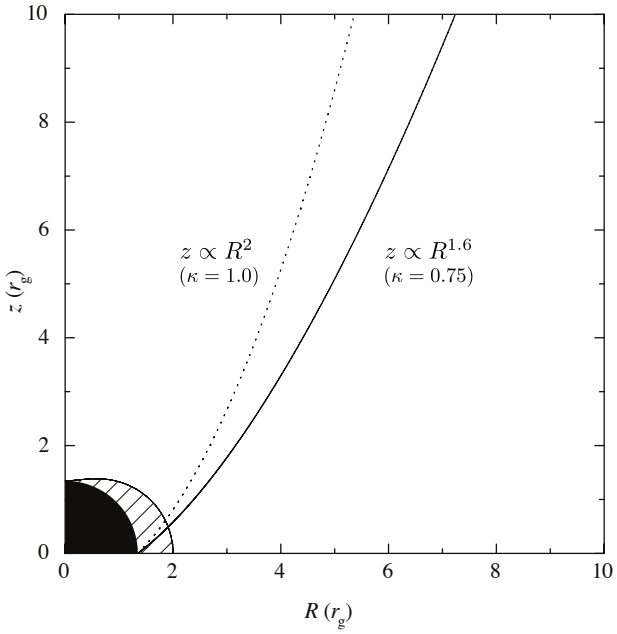

FIG. 1.— Outermost streamlines of the steady axisymmetric solution of the FFE jet (NMF07, TMN08), which are anchored to the event horizon ($r = r_{\rm H}$) with the maximum colatitude angle at the footpoint $\theta_{\rm fp} = \pi/2$. A typical value of $a = 0.9375$ (in GRMHD simulations; Gammie et al. 2004; McKinney & Gammie 2004; McKinney 2006) is specified as a reference. The dotted line show the genuine paraboloidal streamline with $\kappa = 1.0$ ($z \propto R^2$ at $R \gg r_{\rm g}$; e.g. Blandford & Znajek 1977), while the solid line show the paraboloidal streamline with $\kappa = 0.75$ ($z \propto R^{1.6}$ at $R \gg r_{\rm g}$; e.g. Blandford & Payne 1982). The black hole and the ergosphere are represented as the filled and the hatched areas.

In magnetized RIAF simulations about a non-spinning black hole (Igumenshchev 2008), the poloidal magnetic field distribution takes the shape of an "hourglass" shape and has an insignificant vertical component on the equatorial plane outside the black hole. This feature becomes more prominent in the case of spinning black holes as is shown in GRMHD simulations of the ergospheric disk with a vertical magnetic flux (the Wald vacuum solution; Wald 1974); as the poloidal magnetic flux and mass accretes onto the black hole, all magnetic lines threading the ergospheric disk develop a turning point in the equatorial plane resulting in an azimuthal current sheet (Komissarov 2005).

Due to strong inertial frame dragging inside the ergosphere, all plasma entering this region is forced to rotate in the same sense as the black hole. Thus, the poloidal field lines around the equatorial plane are strongly twisted along the azimuthal direction. The equatorial current sheet develops further due to the vertical compression of the poloidal field lines caused by the Lorentz force acting toward the equatorial plane at both upper and lower ($z \gtrless 0$) directions. Magnetic reconnection (although numerical diffusion is responsible for activating the event in an ideal-MHD simulation) will change the field topology; all poloidal field lines entering the ergosphere penetrate the event horizon. A similar result is obtained in GRFFE simulations (Komissarov & McKinney 2007).

We speculate that the situation is qualitatively unchanged even if the weakly magnetized RIAF exists in the system. Strong poloidal fields in the ergosphere compress the innermost black hole accretion flow vertically and reduce the disk thickness down to $H/R \simeq 0.05$, while $H/R \gtrsim 0.3$ (H: the vertical scale height) is the reference value of the disk body outside the plunging region (e.g. Tchekhovskoy 2015).

Based on the physical picture above, we assume no poloidal magnetic flux penetrates the equatorial plane at $R > r_{\rm H}$. Therefore, the outermost field line, which is anchored to the event horizon with the maximum colatitude angle at the footpoint $\theta_{\rm fp} = \pi/2$, can be defined as

$$\Psi(r_{\rm H}, \pi/2) = 1 \tag{3}$$

in Equation (2; e.g., Tchekhovskoy et al. 2008). Figure 1 shows the outermost streamlines of $\Psi(r, \theta) = 1$ with different κ ($\kappa = 1$: BZ77 or $\kappa = 0.75$: BP82) with a fiducial black hole spin ($a = 0.9375$: McKinney & Gammie 2004; McKinney 2006). Let us compare the outermost streamline of the funnel jet in GRMHD simulations with Equation (3) at a quasi-steady state.

2.2. *Our Prospective in GRMHD Simulations*

The public version of the two-dimensional (2D) axisymmetric GRMHD code HARM (Gammie et al. 2003; Noble et al. 2006) is used in our examinations. The code adopts dimensionless units $GM = c = 1$. We, however, occasionally reintroduce factors of c for clarity. Lengths and times are given in units of $r_{\rm g} \equiv GM/c^2$ and $t_{\rm g} \equiv GM/c^3$, respectively. We absorb a factor of $\sqrt{4\pi}$ in our definition of the magnetic field. HARM implements so-called modified Kerr-Schild coordinates: x_0, x_1, x_2, x_3, where $x_0 = t$, $x_3 = \phi$ are the same as in Kerr-Schild coordinates, but the radial $r(x_1)$ and colatitude $\theta(x_2)$ coordinates are modified (McKinney & Gammie 2004). The computational domain is axisymmetric, expanding in the r-direction from $r_{\rm in} = 0.98\, r_{\rm H}$ to $r_{\rm out} = 40\, r_{\rm g}$ and the θ-direction from $\theta = 0$ to $\theta = \pi$. An outflow boundary condition is imposed at $r = r_{\rm out}$; all primitive variables are projected into the ghost zones. The inner boundary condition is identical at $r = r_{\rm in} < r_{\rm H}$ (no back flow into the computational domain). A reflection boundary condition is used at the poles ($\theta = 0$, π).

Typical 2D axisymmetric GRMHD simulations (e.g. Gammie et al. 2003; McKinney & Gammie 2004; McKinney 2006) adopt a dense "Polish Doughnut"-type torus (Fishbone & Moncrief 1976; Abramowicz et al. 1978), which is in a hydrodynamic equilibrium supported by the centrifugal and gas pressure (p) gradient forces. The torus is surrounded by an insubstantial, but dynamic, accreting spherical atmosphere [the rest-mass density ρ and the internal energy density u are prescribed in power-law forms as $\rho_{\rm min} = 10^{-4}(r/r_{\rm in})^{-3/2}$ and $u_{\rm min} = 10^{-6}(r/r_{\rm in})^{-5/2}$] that interacts with the torus. This is the so-called "floor model" that forces a minimum on these quantities in the computational domain to avoid a vacuum. The initial rest-mass density ρ_0 in the system is normalized by the maximum value of the initial torus $\rho_{0,\rm max}$ on the equator.

A poloidal magnetic loop, which is described by the toroidal component of the vector potential as a function of the density $A_\phi \propto \max(\rho_0/\rho_{0,\rm max} - 0.2,\, 0)$, is embedded in the torus. The field strength is normalized with the ratio of gas to magnetic pressure [the so-called plasma-β, hereafter $\beta_{\rm p} \equiv 2(\gamma - 1)u/b^2$, where $b^2/2 = b^\mu b_\mu/2$ is the magnetic pressure measured in the fluid frame]. The inner edge of the torus is fixed at $(r,\, \theta) = (6\, r_{\rm g},\, \pi/2)$ and the pressure maximum is located at $(r,\, \theta) = (r_{\rm max},\, \pi/2)$, where $r_{\rm max} = 12\, r_{\rm g}$ is adopted. $\beta_{\rm p0,min} = 100$, where $\beta_{\rm p0,min}$ denotes the minimum plasma-β at $t = 0$, is chosen[5] for our fiducial run. An

[5] The magnetic field strength is normalized by $\beta_{\rm p0,min}$ by finding the

ideal gas equation of state $p = (\gamma - 1)u$ is used and the ratio of specific heats γ is assumed to be 4/3. If not otherwise specified, a value of $a = 0.9375$ is used (McKinney 2006). For further computational details, readers can refer to Gammie et al. (2003); McKinney & Gammie (2004) which adopt default parameters in HARM.

Given small perturbations in the velocity field, the initial state of a weakly magnetized torus with a minimum value of $\beta_{\rm p0,min} \gtrsim 50$ is unstable against the magneto-rotational instability (MRI; Balbus & Hawley 1991) so that a transport of angular momentum by the MRI causes magnetized material to plunge from the inner edge of the torus into the black hole. The turbulent region in the RIAF's body and corona/wind gradually expands outward. The inner edge of the torus forms a relatively thin disk with the "Keplerian" profile on the equator in both cases of non-spinning (Igumenshchev 2008) and spinning (McKinney & Gammie 2004) black holes. The turbulent inflow of the RIAF body becomes laminar at the plunging region inside the innermost stable circular orbit (ISCO) (e.g. Krolik & Hawley 2002; De Villiers et al. 2003; McKinney & Gammie 2004; Reynolds & Fabian 2008), whereas there is no other specific signature in the flow dynamics across the ISCO (Tchekhovskoy & McKinney 2012). During the time evolution of the system, PFD (highly magnetized, low-density) funnel jets are formed around both polar axes ($\theta = 0$ and π).

Our goal in using GRMHD simulations is to examine the quasi-steady structure of the boundary between the low-density funnel interior (PFD jet) and the high-density funnel exterior (corona/wind outside the RIAF body). It can be directly compared with an outermost streamline of the semi-analytical FFE jet solution, which is anchored to the horizon (Figure 1), when the funnel enters a long, quasi-steady phase.

3. RESULTS

3.1. *Fiducial Run:* $a = 0.9375$

We first examine a high-resolution (fiducial) model in McKinney & Gammie (2004); default parameters in HARM (as introduced above) are adopted with a fine grid assignment $N_{x_1} \times N_{x_2} = 456 \times 456$. The simulation is terminated at $t/t_{\rm g} = 2000$, or about 7.6 orbital periods at the initial pressure maximum on the equator. The MRI turbulence in the RIAF body is not sustained at $t/t_{\rm g} \gtrsim 3000$ due to our assumption of axisymmetry as explained by the anti-dynamo theorem (Cowling 1934). However, the decay of the turbulence does not affect the evolution of the PFD funnel jet (McKinney 2006). Thus, we extended the time evolution up to $t/t_{\rm g} = 9000$ in order to examine whether the quasi-steady state of the PFD funnel jet is obtained or not. This enables us to perform a direct comparison between the steady axisymmetric FFE solution and axisymmetric GRMHD simulations regarding the funnel shape. Constraining physical quantities at the funnel edge is important for further understanding the structure of relativistic jets in M87 and others in general.

Figure 2 shows the time sequence of the distribution of the relative densities of magnetic and rest-mass energy b^2/ρ. This figure provides a quantitative sense for the spatial distribution of the PFD funnel jet, wind/corona, and RIAF body (see also Figures 5 and 7 for details). Following some previous work (e.g. McKinney 2006; Dexter et al. 2012), we confirmed

global maxima of u and b^2 in the computational domain. They lie inside the torus, but not at the same grid point. The magnetic "O-point" is located at the gas pressure maximum on the equatorial plane.

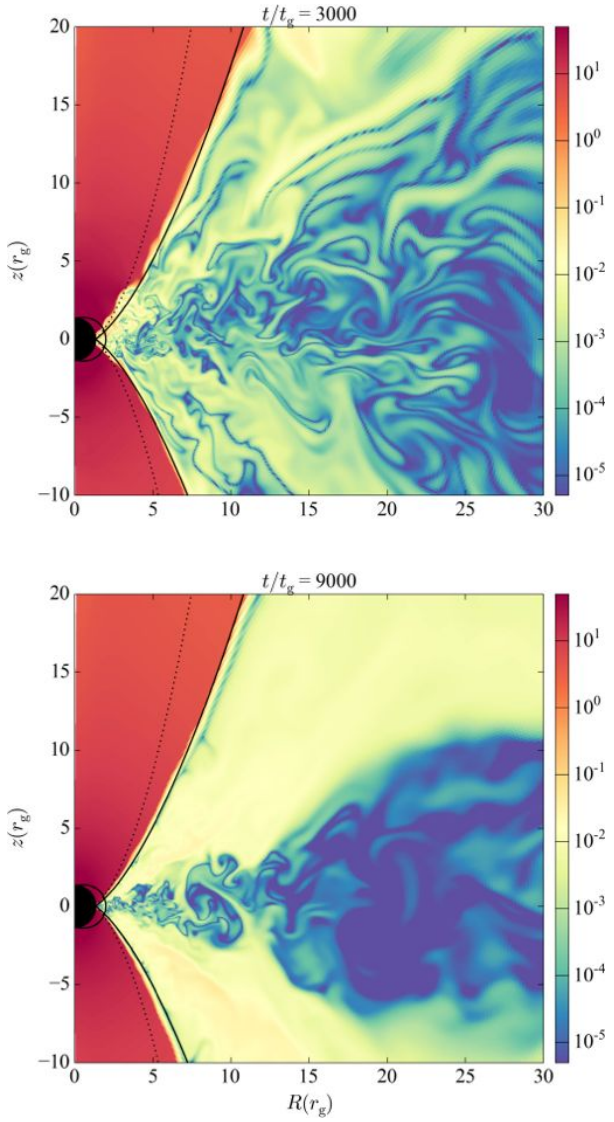

FIG. 2.— Time evolution of the fiducial run ($a = 0.9375$); $t/t_{\rm g} = 3000$ (*top*) and 9000 (*bottom*), respectively. A color filled contour shows the magnetic energy per unit particle b^2/ρ, which is measured in the fluid frame. The black hole, the ergosphere ("not hatched"), and two outermost streamlines (genuine parabolic/parabolic), which are anchored to the event horizon, are displayed in the same manner as in Figure 1.

that the funnel jet-wind/corona boundary can be identified to be where $b^2/\rho \simeq 1$. At the stage $t/t_{\rm g} = 3000$ (*top* panel), the MRI is well developed and thus the magnetized material in the RIAF body is swallowed by the black hole. A certain amount of the poloidal flux, which falls into the ergosphere, is twisted along the azimuthal direction and powerful PFD jets are formed toward the polar directions. Consequently, the funnel expands laterally by the magnetic pressure gradient and its outer boundary ($b^2/\rho \simeq 1$; orange between red and yellow on the contour map) shapes a non-conical geometry, which is quantitatively similar to the parabolic outermost streamline (thick solid line) $z \propto R^{1.6}$ (BP82; see Figure 1).

After this phase, the MRI-driven turbulence in the wind/corona region above the RIAF body decays gradually. The *bottom* panel shows the final stage ($t/t_{\rm g} = 9000$) of the system; the turbulent structure is saturated in the wind/corona region, but it survives near the equator in the RIAF body. It is notable that the BP82-type parabolic structure of the fun-

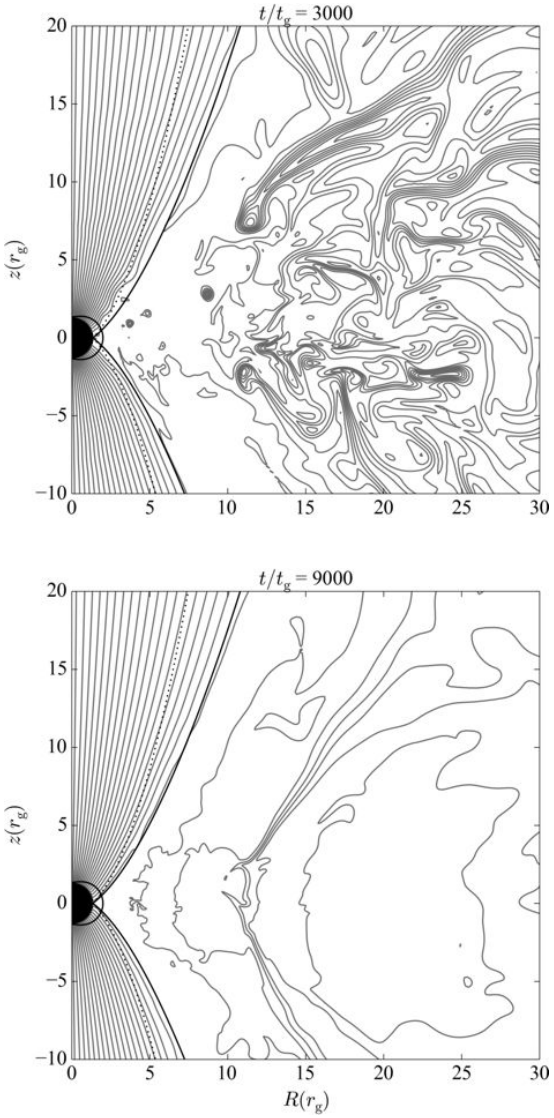

FIG. 3.— Time evolution of the fiducial run ($a = 0.9375$); $t/t_g = 3000$ (*top*) and 9000 (*bottom*), respectively. Contours (gray) represent poloidal magnetic field lines. Other components in the panels are identical to those in Figure 2.

nel jet-corona/wind boundary is still sustained until this phase (unchanged at the quantitative level during $t/t_g \simeq 3000$–9000), suggesting the PFD funnel jet is entering a quasi-steady state, while the outside region (wind/corona and RIAF body) still evolves dynamically. The distribution of b^2/ρ can be divided into the following three regions; i) the funnel ($\gtrsim 1$), ii) the wind/corona ($\simeq 10^{-3}$–10^{-1}), and iii) the RIAF body ($\lesssim 10^{-3}$), respectively. Thus, we clearly identified that the PFD funnel jet (orange to red) is outlined with the BP82-type parabolic shape, rather than the genuine parabolic shape (BZ77: $z \propto R^2$). It is also notable that the boundary of the funnel follows $b^2/\rho \simeq 1$ during the whole time of the quasi-steady state at $t/t_g \gtrsim 3000$.

Figure 3 displays the poloidal magnetic field line distribution at the same times chosen for Figure 2. We can see that the ordered, large-scale poloidal magnetic flux only exists inside the PFD funnel jet region where $b^2/\rho \gtrsim 1$ (Figure 2) during the quasi-steady state $t/t_g \gtrsim 3000$. There seems to be no such coherent poloidal magnetic flux penetrating the equatorial plane at $R > r_H$. This is also examined in Komissarov (2005); Komissarov & McKinney (2007). At the stage $t/t_g = 3000$, a lateral alignment of the poloidal magnetic flux ends at around the outermost parabolic streamline $z \propto R^{1.6}$. This holds until the final stage of $t/t_g = 9000$. Thus, the distribution of poloidal magnetic field lines also indicates the funnel interior reaches a quasi-steady state with insignificant deviation when $t/t_g \gtrsim 3000$.

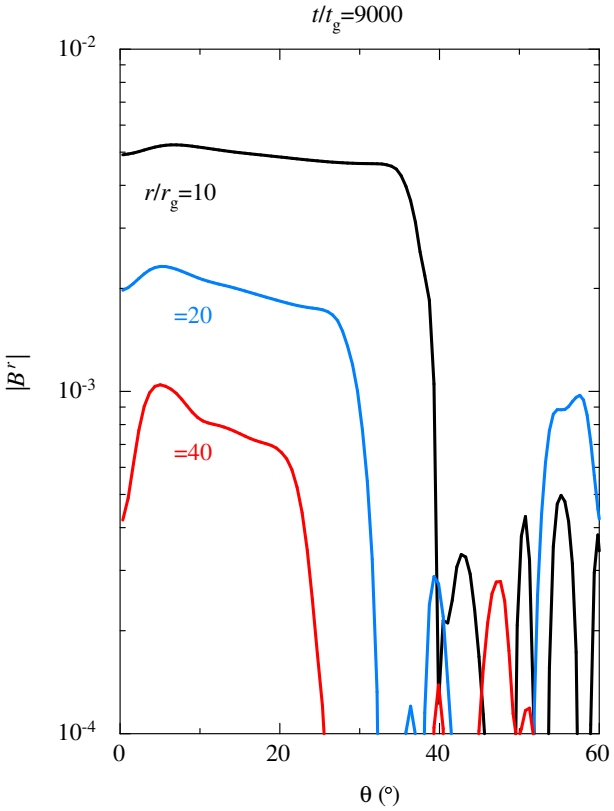

FIG. 4.— A θ cross-section at r/r_g =10 (black), 20 (blue), and 40 (red) showing the absolute value of the radial magnetic field $|B^r|$ in the fiducial run ($a = 0.9375$) at $t/t_g = 9000$.

The density of contours in Figure 3 directly represents the poloidal field strength (it may be a quantitatively reasonable interpretation at least in the funnel area). At the interior of the funnel jet, the lateral spacing of each field line decreases ($R/r_g \to 0$) at around the event horizon ($r/r_g \lesssim$ a few), suggesting an accumulation of the poloidal flux around the polar axis (z). This is caused by the enhanced magnetic hoop stress by the toroidal field component and it is prominent if the black hole spin becomes large ($a \to 1$; Tchekhovskoy et al. 2010). On the other hand, we may also see this effect in the downstream region ($r/r_g \lesssim 20$) along the polar axis, but a concentration of the poloidal flux is rather smooth and weak compared with the innermost region around the event horizon. It indicates that the toroidal field does not yet fully dominate the poloidal one on this scale and no effective bunching of the poloidal flux takes place (cf. Figure 9 for a visible inhomogeneity further downstream). Figure 4 confirms this quantitatively; a concentration of the poloidal magnetic field becomes clear as r increases (at $r/r_g \gtrsim 20$ and $\theta \lesssim 20°$). We can also identify the gradual decrease of $|B^r|$ as a function of θ, implying a differential bunching of the poloidal flux. Further examinations are presented in Section 3.2.2 (behaviors at the downstream in our large domain computations with different

black hole spins).

No visible (but very weak) bunching of poloidal magnetic flux at a few $\lesssim r/r_{\rm g} \lesssim 20$ (see *middle* and *bottom* panels in Figure 3) indicates that the local poloidal field can be approximately treated as a force-free system (Narayan et al. 2009). It is worth noting that the radial (r) distribution of b^2/ρ inside the funnel jet has a weak dependence on the colatitude angle (θ), as is shown in Figure 2. This also implies no effective bunching of the poloidal flux as well as no concentration of the mass density toward the polar axis. We consider that a quasi-uniform stratification of b^2/ρ inside the funnel (near the event horizon) plays a critical role in determining the dynamics of the GRMHD jet (the lateral stratification of the bulk acceleration), as is treated in Sections 3.2.2, 3.2.3, and 5.2.

In order to confirm the boundary between the PFD funnel jet and the wind/corona region at a quantitative level, we provide Figure 5; Contours of $b^2/\rho = 1$ and $\beta_{\rm p} = 1$ are shown, at the final stage of $t/t_{\rm g} = 9000$ during the long-term, quasi-steady state ($t/t_{\rm g} \gtrsim 3000$) in our fiducial run. It is similar to Figure 2 in McKinney & Gammie (2004) and Figures 3 in McKinney (2006). Note that their snapshots correspond to $t/t_{\rm g} \leq 2000$, which is before when we find the funnel reaches a quasi-steady state. Notably, the equipartition of these quantities ($b^2/\rho = 1$ and $\beta_{\rm p} = 1$) is maintained at the funnel edge along the outermost BP82-type parabolic streamline. There are other contours of $\beta_{\rm p} = 1$, which are distributed outside the funnel and above the equatorial plane. Quantitatively, the latter corresponds to the boundary between the wind/corona and the RIAF body ($\beta_{\rm p} = 3$; e.g. McKinney & Gammie 2004; McKinney 2006).

We also identify the boundary between the PFD funnel jet and the external area (wind/corona and RIAF body) regarding the unbound/bound state of the fluid to the black hole by means of the Bernoulli parameter (e.g. De Villiers et al. 2003; McKinney & Gammie 2004): $Be = -hu_t - 1$, where $h = 1+(u+p)/\rho$ is the relativistic specific enthalpy and u_t is the covariant time component of the plasma 4-velocity. In the fiducial run (and other runs as well in the next section), we confirm $p/\rho \lesssim 10^{-1}$ throughout the computational domain. Thus, we can approximately use $h \approx 1$ and $Be \approx -u_t - 1$, which is adopted throughout this paper. A fluid is gravitationally unbound and can escape to infinity for $Be > 0$, and vice versa. The contour of $-u_t = 1$ ($Be \approx 0$) is shown in Figure 5, forming "V"-shaped geometry (originally found in McKinney & Gammie 2004). We can clearly find the bound region $Be < 0$ inside the PFD funnel (close to the black hole) and whole outside (throughout the computational domain $r/r_{\rm g} \leq 40$). It is a well-known issue, though we emphasize here, that the outgoing mass flux in the PFD funnel jet does *NOT* come from the event horizon, whereas the Poynting flux is extracted from there via the Blandford-Znajek process (Blandford & Znajek 1977) as is widely examined (e.g. McKinney & Gammie 2004; McKinney 2006; Globus & Levinson 2013; Pu et al. 2015).

As investigated above, our fiducial run provides the boundary condition of the funnel edge (at a quantitative level);

$$b^2/\rho \simeq 1,\ \beta_{\rm p} \simeq 1,\ \text{and}\ -u_t \simeq 1\ (Be \approx 0) \qquad (4)$$

along the outermost BP82-type parabolic ($z \propto r^{1.6}$) streamline (the ordered, large-scale poloidal magnetic field line), which is anchored to the event horizon with the maximum colatitude angle $\theta_{\rm fp} \simeq \pi/2$ (at the footpoint). There is a discrepant distribution of these quantities in previous results

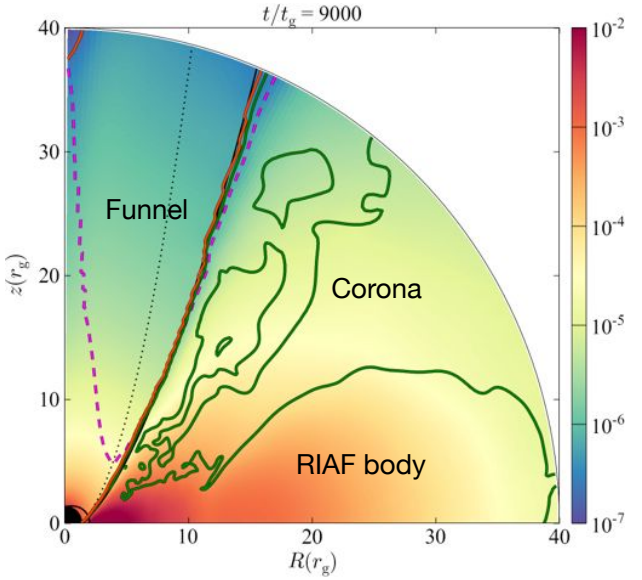

FIG. 5.— The final snapshot of the fiducial run ($a = 0.9375$); $t/t_{\rm g} = 9000$. A color filled contour shows the total pressure $p + b^2/2$ (in the fluid frame). Contours of equipartition quantities are exhibited (the upper computational domain; $0 \leq \theta \leq \pi/2$). An orange solid line shows $b^2/\rho = 1$, while green solid lines show $\beta_{\rm p} = 1$. $-u_t = 1$ ($Be \approx 0$) is shown with a magenta dashed line. Other components are identical to those in Figure 2.

(McKinney & Gammie 2004; McKinney 2006). We speculate this may be just because the funnel does not reach a quasi-steady state. Note that an alignment of the funnel edge along the specific streamline depends weakly on the initial condition (such as $\beta_{\rm p0,min}$); formation of a BP82-type parabolic funnel is confirmed for a reasonable range of $50 \lesssim \beta_{\rm p0,min} < 500$ under the fixed Kerr parameter ($a = 0.9$) up to $r_{\rm out}/r_{\rm g} = 100$ (see Appendix A). We also note that a qualitatively similar structure of the low-density funnel edge of $b^2/\rho \simeq 1$, which is anchored to the event horizon with a high inclination angle $\theta > 80°$, is identified in three-dimensional (3D) GRMHD simulations with $a = 0.5$ (e.g. Ressler et al. 2017). Thus, we suggest our finding may not depend on the dimensionality (2D or 3D).

We further examine the distribution of the total (gas + magnetic) pressure, which is underlaid in Figure 5. It gives a good sense of the jet confinement by the ambient medium. External coronal pressure outside the funnel, which consists of both gas and magnetic contributions ($\beta_{\rm p} \simeq 1$), is surely overpressured with respect to the magnetic pressure-dominated region ($\beta_{\rm p} \ll 1$) inside the funnel. The situation seems unchanged even after the MRI-driven MHD turbulence saturates as is shown in Figure 6. In the vicinity of the black hole ($r/r_{\rm g} \lesssim 5$), the total pressure of the RIAF body, which is dominated by the gas pressure ($t/t_{\rm g} \lesssim 3000$) or in an equipartition ($\beta_{\rm p} \sim 1$; $t/t_{\rm g} \gtrsim 3000$). The important point of Figure 6 is that the funnel pressure (magnetically dominated) and the coronal pressure ($\beta_{\rm p} \simeq 1$) are almost unchanged during $t/t_{\rm g} \simeq 3000$–9000, suggesting the quasi-steady parabolic shape of the funnel is sustained. Some convenient terminology is provided in Figure 5 for dividing the domain into the funnel ($b^2/\rho \gg 1$, $\beta_{\rm p} \ll 1$), corona ($b^2/\rho \simeq 10^{-2}$, $\beta_{\rm p} \simeq 1$), and RIAF body ($b^2/\rho \ll 10^{-2}$, $\beta_{\rm p} \gtrsim 1$), following the literature (De Villiers et al. 2003; McKinney & Gammie 2004; Hawley & Krolik 2006; Sadowski et al. 2013).

We realize, *however*, that the ram pressure of the accreting gas becomes even higher than the total pressure in the RIAF

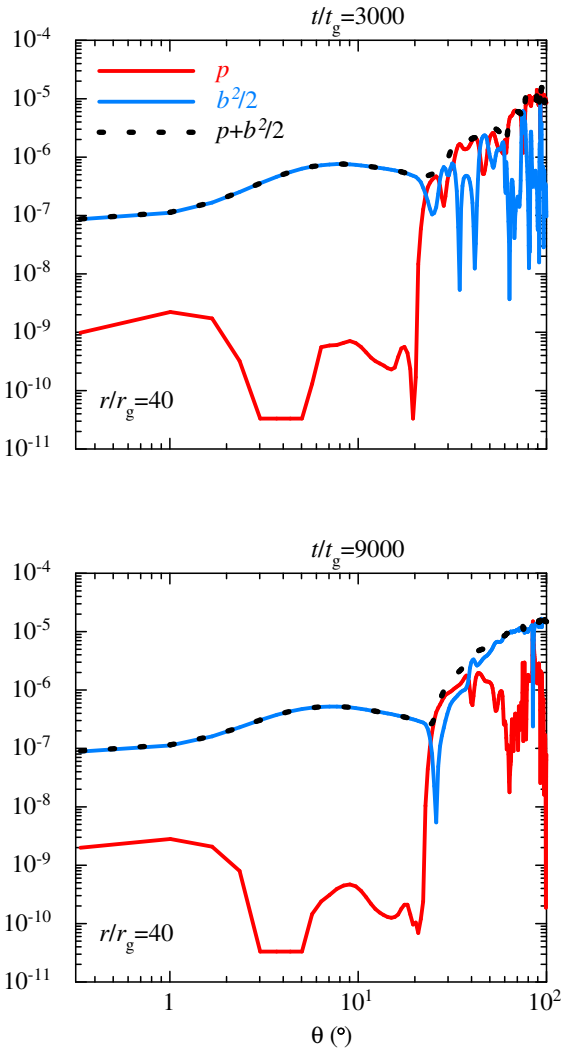

FIG. 6.— A θ cross-section at $r/r_{\rm g} = 40$ showing the gas pressure (red solid line), the magnetic pressure (blue solid line), and their sum (the total pressure: black dotted line) in the fiducial run ($a = 0.9375$); $t/t_{\rm g} = 3000$ (*top*) and 9000 (*bottom*).

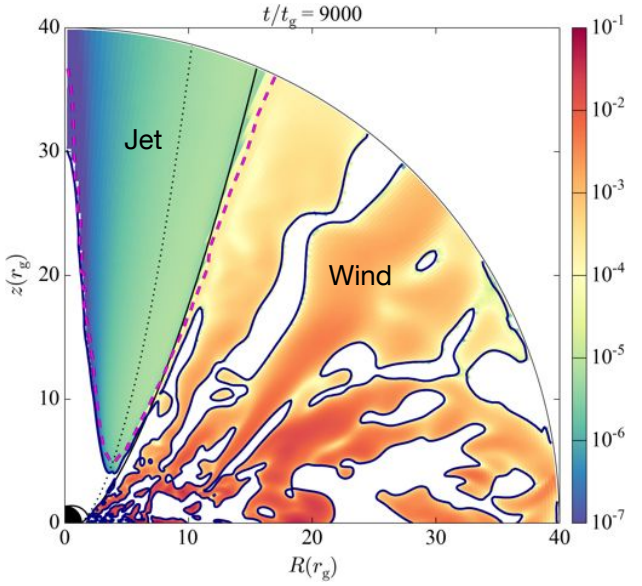

FIG. 7.— The final snapshot of the fiducial run ($a = 0.9375$); $t/t_{\rm g} = 9000$. The magnitude of the outgoing radial mass flux density $\sqrt{-g}\rho u^r (> 0)$, where u^r is the radial component of the four-velocity, $\sqrt{-g} = \Sigma \sin\theta$ is the metric determinant, and $\Sigma \equiv r^2 + a^2\cos^2\theta$, is shown with a color filled contour (the upper computational domain; $0 \le \theta \le \pi/2$). Contours with navy solid lines show $u^r = 0$, while "whiteout" regions indicate the magnitude of the ingoing radial mass flux density $\sqrt{-g}\rho u^r (< 0)$. The jet stagnation surface is clearly displayed inside the PFD funnel ($u^r = 0$). $-u_t = 1$ ($Be \approx 0$) is shown with a magenta dashed line. Other components are identical to those in Figure 2.

body on the equatorial plane (by almost an order of magnitude). This is conceptually similar to the so-called "magnetically arrested disk" (MAD: e.g. Narayan et al. 2003; Igumenshchev 2008; Tchekhovskoy et al. 2011) although the accretion flow in our HARM fiducial run is identified as the "standard and normal evolution" (SANE: Narayan et al. 2012) without having an arrested poloidal magnetic flux on the equatorial plane at $R > r_{\rm H}$ (see Figure 3). Anyhow, as a consequence of this combination of effects, we could expect that the PFD jet to be deformed into a non-conical geometry. Note that the funnel structure becomes radial (i.e., conical) if the magnetic pressure in the funnel is in equilibrium with the total pressure in the corona and the RIAF body in 3D GRMHD simulations (e.g. Hirose et al. 2004). We also remark that the low-density funnel edge with $b^2/\rho \simeq 1$ is established even in the MAD state with 3D runs (Ressler et al. 2017).

Finally, Figure 7 provides further examination of outflows (and inflows as well) in the system. The outgoing radial mass flux density exists both inside and outside the funnel, but that in the corona is significantly higher than the funnel with ~ 1–3 orders of magnitude, which is quantitatively consistent with other 3D simulations in the SANE state (e.g. Sadowski et al. 2013; Yuan et al. 2015). Aside from the terminology in McKinney & Gammie (2004), we consider outflows in the funnel as jets, while those in the corona as winds (e.g. Sadowski et al. 2013), as is labeled. The former is highly magnetized with considerable poloidal magnetic flux and powered by the spinning black hole, but the latter is not (see, Figures 2 and 3). A division boundary of these outflows lies on $Be \approx 0$ contour along the outermost BP82-type parabolic streamline. That is, the black hole-driven PFD funnel jet is unbound, but the RIAF-driven coronal wind is bound (at least in our simulation up to $r_{\rm out}/r_{\rm g} = 100$).

In the coronal wind (bound), a considerable mass is supplied from the RIAF and thus the outflow does not possess sufficient energy to overcome the gravitational potential. On the other hand, the funnel jet (unbound), which carries very little mass, becomes relativistic quite easily (due to the magnetic acceleration along the poloidal magnetic field) and could escape to infinity. However, the bound wind may not exist permanently at large distance; Be is presumably not a constant (in the non-steady flow) and the sign can be positive with a 3D turbulent environment (Yuan et al. 2015). The jet stagnation surface in the PFD funnel, at which the contravariant radial component of the plasma 4-velocity becomes zero ($u^r = 0$; McKinney 2006; Pu et al. 2015; Broderick & Tchekhovskoy 2015), is clearly identified.

In Figure 7, we can see that the jet stagnation surface does reasonably coincide with the bound/unbound boundary: $Be \approx 0$ ($-u_t = 1$) except for the polar region ($\theta \sim 0$) of the V-shaped geometry. Outside the PFD funnel jet, the coronal wind can be identified with the outgoing radial mass flux density , but there is an accreting gas (identified by the ingoing radial mass flux density) around $\theta \simeq \pi/4$. On the

other hand, there is the outgoing gas in the RIAF body at $\pi/3 \lesssim \theta \lesssim 2/3\pi$ (see Figure 5). This is not a wind, but associated with turbulent motions. Thus, both inflows and outflows are mixed up in the corona and RIAF body, suggesting the adiabatic inflow-outflow solution (ADIOS: Blandford & Begelman 1999, 2004). Note that u^r does not vanish along the jet/wind boundary and thus the wind plays a dynamical role in confining the PFD jet (see also Figure 11).

The origin of the wind is beyond the scope of our consideration here, but the magneto-centrifugal mechanism (BP82) would be unlikely to operate; it is because of the absence of a coherent poloidal magnet field outside the PFD funnel (see Figure 3), where the toroidal magnetic field is dominant and the plasma is not highly magnetized ($b^2/\rho \ll 1$ and $\beta_{\rm p} \gtrsim 1$; see Figures 2 and 5). Note that a dominant toroidal magnetic field may be also true in the SANE state with 3D runs (e.g. Hirose et al. 2004). Regarding the funnel-wall jet (Hawley & Krolik 2006), which could be driven by a high-total pressure corona squeezing material against an inner centrifugal wall, does not seem to appear in our fiducial simulation. We do not find any significant evidence of it; no pileup of the mass flux and/or the total pressure at the funnel edge along the BP82-type parabolic outermost streamline. There is a key difference between the coronal wind and the funnel-wall jet; the former is bound, while the later is unbound at least in the vicinity of the black hole (De Villiers et al. 2003). The outer boundary of the matter-dominated coronal wind ($b^2/\rho < 0.1$; see Figures 2 and 7) is somewhat indistinct as is indicated by Hawley & Krolik (2006).

3.2. *Parameter Survey: (In)dependence on Black Hole Spins*

Based on our fiducial run, we further examine the BP82-type parabolic structure ($z \propto R^{1.6}$) of the PFD funnel jet against the varying black hole spin. Different Kerr parameters are examined with same value of $\beta_{\rm p0,min} = 100$ in the extended computational domain $r_{\rm out}/r_{\rm g} = 100$ (with a grid assignment $N_{x_1} \times N_{x_2} = 512 \times 512$). We prescribe $r_{\rm max}/r_{\rm g}$=12.95, 12.45, 12.05, and 11.95, for $a = 0.5, 0.7, 0.9$, and 0.99, respectively.

3.2.1. *Funnel Structure*

Figure 8 exhibits b^2/ρ at the final stage $t/t_{\rm g} = 12000$ for various black hole spins. First of all, we confirmed that the overall structure outside the funnel seems to be unchanged with different spins; $b^2/\rho \simeq 10^{-3}$–10^{-1} is obtained in the wind/corona region, while the RIAF body sustains $b^2/\rho \lesssim 10^{-3}$. The MRI-driven turbulence has decayed in both the wind/corona and RIAF body by this phase. The funnel boundary fairly follows the outermost BP82-type parabolic streamline, which is anchored to $r = r_{\rm H}$, but shifts inward with increasing a (the funnel becomes "slimmer"). We find that $b^2/\rho \simeq 1$ is maintained along the funnel edge for sufficiently high spins ($a \geq 0.9$), while the value is somewhat smaller—around $b^2/\rho \simeq 0.5$—for lower spins ($a \leq 0.7$) in the quasi-steady phase; $b^2/\rho \leq 5$ is obtained at the jet stagnation surface (see Figure 14 in the next section) so that the downstream of the funnel jet does not hold a highly PFD state.

We report one obvious, but notable dependence on the black hole spin a during the time evolution of the system in Figure 8; b^2/ρ in the funnel grows larger when a increases. This implies that a large spin would be suitable for obtaining a large value of b^2/ρ at the jet launching region, which determines the maximum Lorentz factor (e.g. McKinney 2006, see also Figure 14 for reference values). Thus, we may consider the black hole spin dependence on the asymptotic Lorentz factor at large distance although another factor (i.e., the magnetic nozzle effect) may also affect this. Beneath the jet stagnation surface, there is an inflow $u^r < 0$ ($Be < 0$) along each streamline because the fluid is strongly bound by the hole's gravity. Thus, a shift of the jet stagnation can be expected, depending on the black hope spin; the fluid can escape from a deeper gravitational potential well of the hole due to an enhanced magneto-centrifugal effect in a cold GRMHD flow (Takahashi et al. 1990; Pu et al. 2015) if a becomes large. See Section 3.2.3 with Figures 14 for more details.

On the other hand, we confirmed that the shape of the funnel exhibits a weak dependence on the black hole spin ($a \geq 0.5$). As a increases, the angular frequency Ω of a poloidal magnetic field line (Ferraro 1937) increases where frame dragging is so large inside the ergosphere that it generates a considerably larger toroidal magnetic field. Consequently, a magnetic tension force due to hoop stresses ("magnetic pinch") would be expected to act more effectively on collimating the funnel jet. It, however, is not the case at the funnel edge; hoop stresses nearly cancel centrifugal forces, suggesting that a self-collimation is negligible (McKinney & Narayan 2007a,b). Note that a self-collimation will be effective at the funnel interior as a increases (see below).

As is introduced in Section 2.1, the outermost BP82-type parabolic streamline ($z \propto R^{1.6}$) of the steady axisymmetric FFE jet solution (NMF07, TMN08), which is anchored to the event horizon with the maximum colatitude angle $\theta_{\rm fp} = \pi/2$, can suitably represent the boundary (Equation 3) between the PFD funnel jet and the wind/corona region. The funnel edge can be approximately defined as the location where $b^2/\rho \simeq 0.5$–1 along the specific curvilinear shape. This is, at least in our GRMHD simulations, valid on the scale of $r/r_{\rm g} \lesssim 100$ with a range of Kerr parameters $a = 0.5$–0.99 (due to the limited space, we omit to show the case of $a = 0.998$, but we confirmed similar structure of the PFD funnel jet as is shown in Figure 8). Again, we report a formation of the BP82-type parabolic funnel with $50 \lesssim \beta_{\rm p0,min} < 500$ ($a = 0.9$) up to $r_{\rm out}/r_{\rm g} = 100$ in our GRMHD runs (see Appendix A).

Figure 9 displays the poloidal magnetic field lines, corresponding to each panel of Figure 8. We obtained qualitatively similar results with Figure 3 at the final stage ($t/t_{\rm g} = 9000$) and the overall feature is unchanged with varying the black hole spin as is similar to Figure 8. Again, there is no coherent structure of the poloidal magnetic field lines in both the corona and RIAF body for all cases: $a = 0.5$-0.99. It is likely that the MHD turbulence (due to the MRI) saturates in our axisymmetric simulations, whereas there are some features of poloidal field tangling. As is widely examined in a 3D simulation with similar initial weak poloidal field loops lying inside the torus, the evolved field is primarily toroidal in the RIAF body and corona (e.g. Hirose et al. 2004); the magnetic energy of the coronal field is, on average, in equipartition with the thermal energy ($\beta_{\rm p} \simeq 1$) and the corona does not become a magnetically dominated force-free state, which is quantitatively consistent with our results.

By contrast, in the funnel region ($b^2/\rho \gtrsim 1$) the field is essentially "helical" with a dominant radial component outside the ergosphere and a toroidal component that becomes larger with increasing black hole spin (see also Hirose et al. 2004). In their result, the magnetic pressure in the funnel is in equilibrium with the total pressure in the corona and the inner part of the RIAF body. This is, however, different form

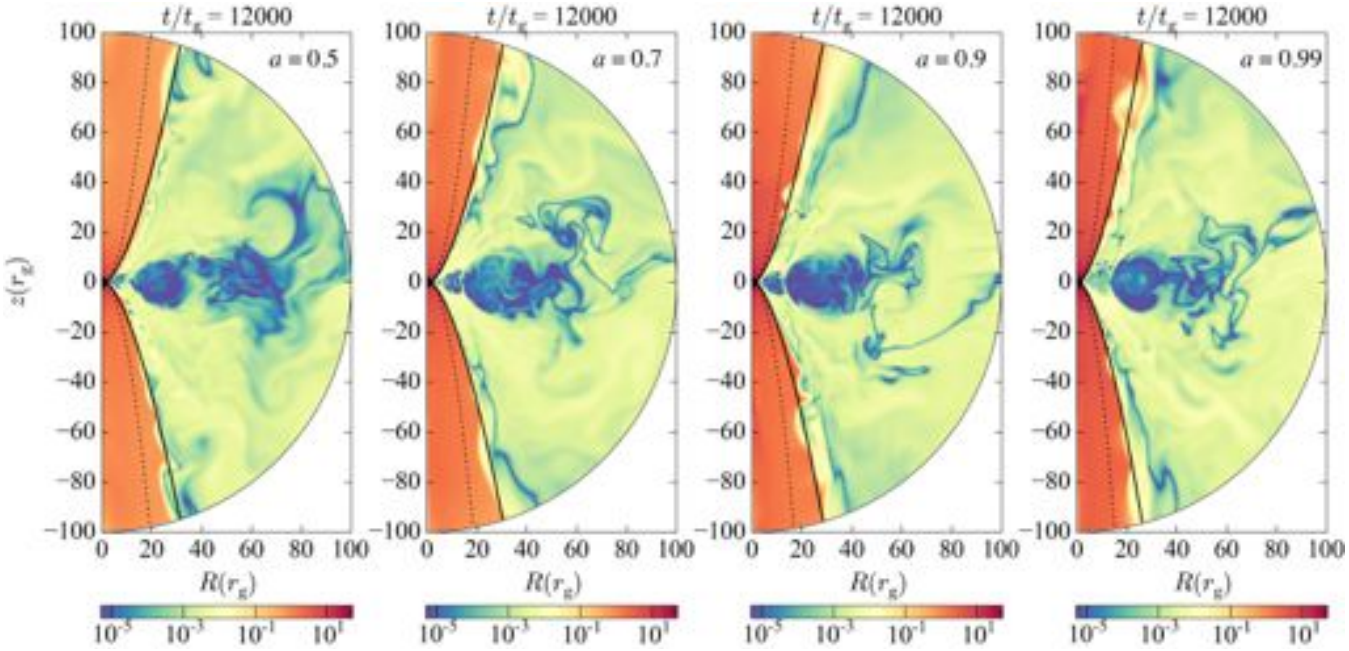

FIG. 8.— A color filled contour of b^2/ρ for four different runs with different black hole spins (from *left* to *right*: $a = 0.5$, 0.7, 0.9, and 0.99). The final snapshot ($t/t_g = 12000$) is displayed for each run with the whole computational domain $r/r_g \leq 100$ and $0 \leq \theta \leq \pi$. Other components in panels are identical to those in Figure 1, but the black hole spin is adjusted.

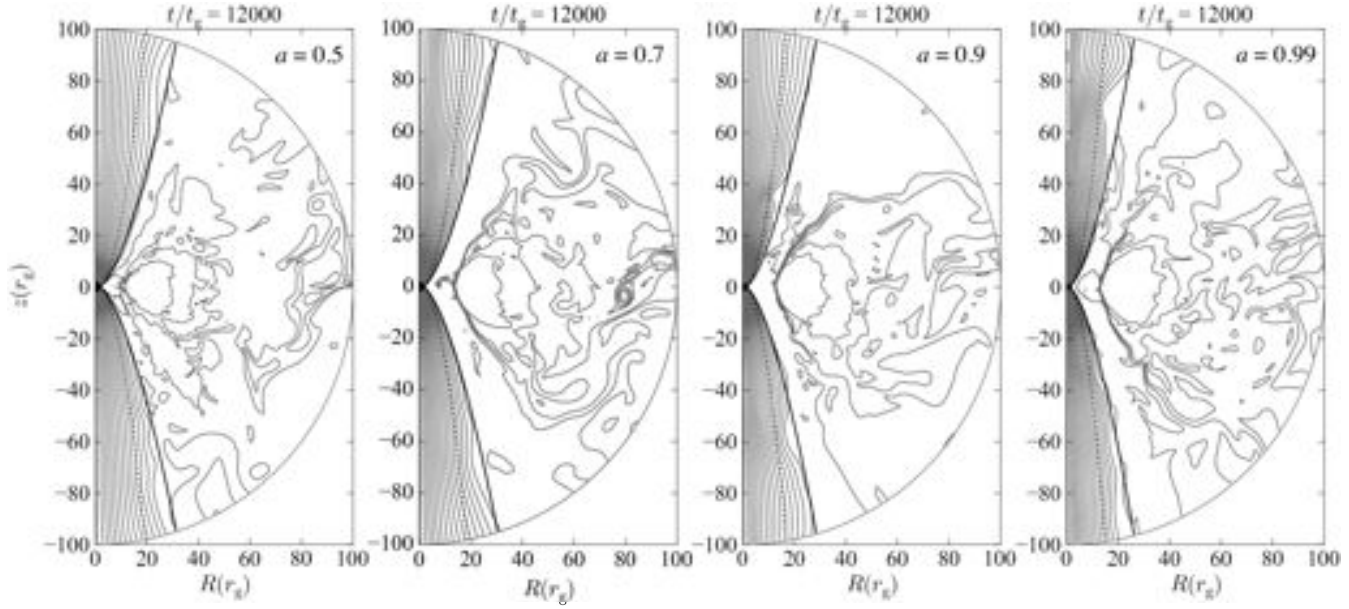

FIG. 9.— Contours (gray) show poloidal magnetic field lines for four different runs with different black hole spins (from *left* to *right*: $a = 0.5$, 0.7, 0.9, and 0.99). The final snapshot ($t/t_g = 12000$) is displayed for each run with the whole computational domain $r/r_g \leq 100$ and $0 \leq \theta \leq \pi$. Other components in panels are identical to those in Figure 8.

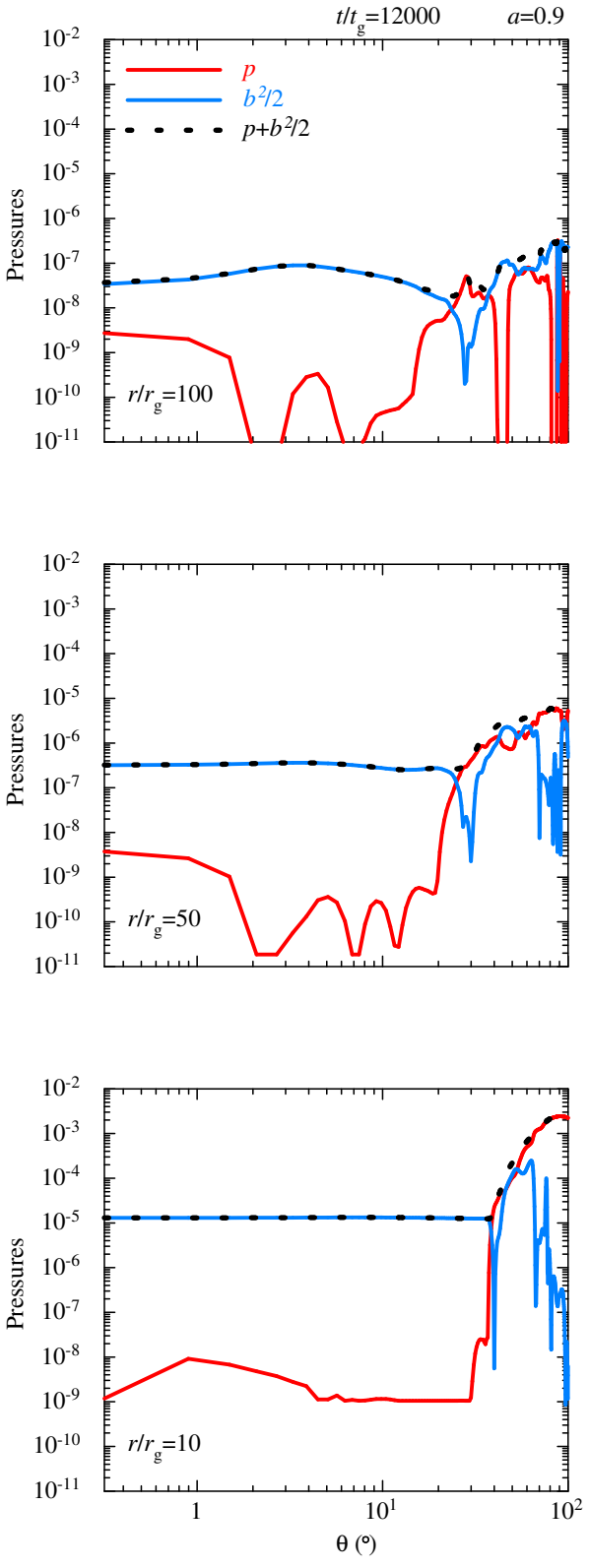

FIG. 10.— A θ cross-section showing the gas pressure (red solid line), the magnetic pressure (blue solid line), and their sum (the total pressure: black dotted line) at the final stage ($t/t_{\rm g} = 12000$) for $a = 0.9$; $r/r_{\rm g} = 100$ (*top*), 50 (*middle*), and 10 (*bottom*).

our results; as is shown in our fiducial run (Figure 5), the total pressure in the PFD funnel (i.e., the dominant magnetic pressure) is smaller than the outer total pressure (especially at $r/r_{\rm g} \lesssim$ 20-30, where the curvature of the funnel edge is large). We understand that this is one of the reasons why our PFD funnel jet is deformed into a paraboloidal configuration, rather than maintaining the radial shape.

Figure 10 shows that an excess of the external coronal pressure (compared with the funnel pressure) gradually decreases as r increases (as the curvature of the parabolic funnel becomes small). They are almost comparable at $r/r_{\rm g} = 100$, indicating that the pressure balance is established, where the magnetic pressure inside the funnel decays about two orders of magnitude compared with that at $r/r_{\rm g} = 10$. By combining with Figure 11, it is implied that a coronal wind plays a dynamical role in shaping the jet into a parabolic geometry.

An inhomogeneous spacing of poloidal magnetic field lines in the lateral direction (R) at $z/r_{\rm g} \gtrsim 50$ (the tendency becomes strong with $a \geq 0.7$) is confirmed in Figure 9 (the density of contours is high around the polar axis, while it becomes low near the funnel edge). This is widely seen in the literature and interpreted as the self-collimation by the magnetic hoop stress, which collimates the inner part of streamlines relative to the outer part (e.g. Nakamura et al. 2006; Komissarov et al. 2007, 2009; Tchekhovskoy et al. 2008, 2009, 2010). This is named as "differential bunching/collimation" of the poloidal magnetic flux (Tchekhovskoy et al. 2009; Komissarov et al. 2009), leading to a sufficient opening of neighboring streamlines for an effective bulk acceleration via the magnetic nozzle effect (e.g. Toma & Takahara 2013, for recent progress and references therein). In the next section, further quantitative examination of the differential bunching of the poloidal magnetic flux is presented (see also Figure 13), which is associated to the jet bulk acceleration.

3.2.2. *Outflows*

Next, we examine the nature of the coronal wind in Figure 11, corresponding to each panel of Figure 8. Again, we obtain qualitatively similar results with Figure 7 (the magnitude of the outgoing radial mass flux density of the coronal wind is higher than that of the funnel jet by $\sim$ 1–3 orders of magnitude) even as the black hole spin varies. This is consistent with the SANE state of 3D GRMHD simulations, in which the magnitude of the outgoing radial mass flux density of the coronal wind does not exhibit a noticeable dependence on the black hole spin (Sadowski et al. 2013). We also confirm the distribution of $Be \approx 0$ ($-u_t = 1$) forms a V-shaped geometry as mentioned in Section 3.1. The right side of the V-shaped distribution of $Be \approx 0$ reasonably follows the outermost BP82-type parabolic streamline, which is anchored to the event horizon, up to $r_{\rm out}/r_{\rm g} = 100$ for $a = 0.5$–0.99 (although there is some deviation near the outer radial boundary in $a = 0.9$), suggesting that the coronal wind is bound up to $r_{\rm out}/r_{\rm g} \sim 100$. It is notable that the jet stagnation surface ($u^r = 0$) inside the funnel shifts towards the black hole as a increases (e.g. Takahashi et al. 1990; Pu et al. 2015), but it coincides with the left side of the V-shaped distribution of $Be \approx 0$ except for the polar region ($\theta \sim 0$; see also Figure 7).

Finally, we examine the velocity of the funnel jet. We evaluate the Lorentz factor Γ, which is measured in Boyer-Lindquist coordinates (e.g. McKinney 2006; Pu et al. 2015);

$$\Gamma = \sqrt{-g_{tt}}u^t, \quad (5)$$

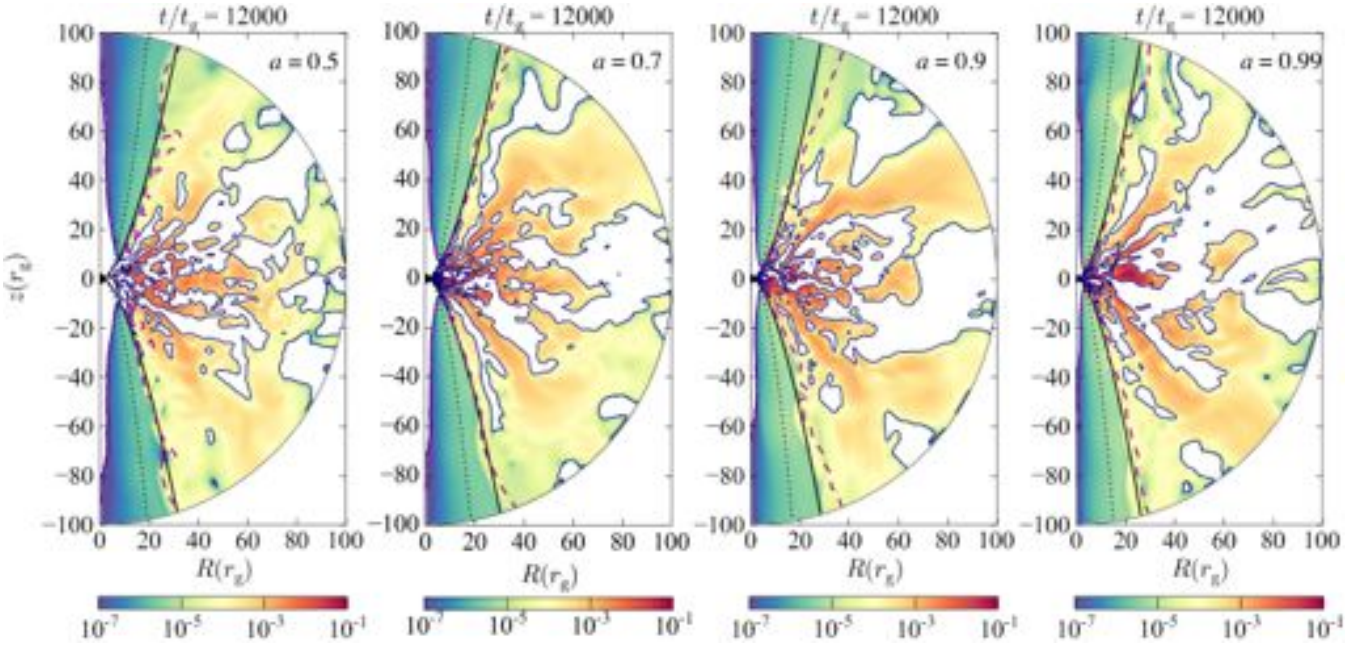

FIG. 11.— A color filled contour of the magnitude of the outgoing radial mass flux density (similar to Figure 7) for four different runs with different black hole spins (from *left* to *right*: $a = 0.5$, 0.7, 0.9, and 0.99). The final snapshot ($t/t_g = 12000$) is displayed for each run with the whole computational domain $r/r_g \leq 100$ and $0 \leq \theta \leq \pi$. Navy solid line shows $u^r = 0$, while "whiteout" regions indicate the magnitude of the ingoing radial mass flux density. The jet stagnation is clearly displayed inside the PFD funnel ($u^r = 0$), and it shifts towards the black hole when a increases. $-u_t = 1$ ($Be \approx 0$) is shown with a magenta dashed line. Other components in panels are identical to those in Figure 8.

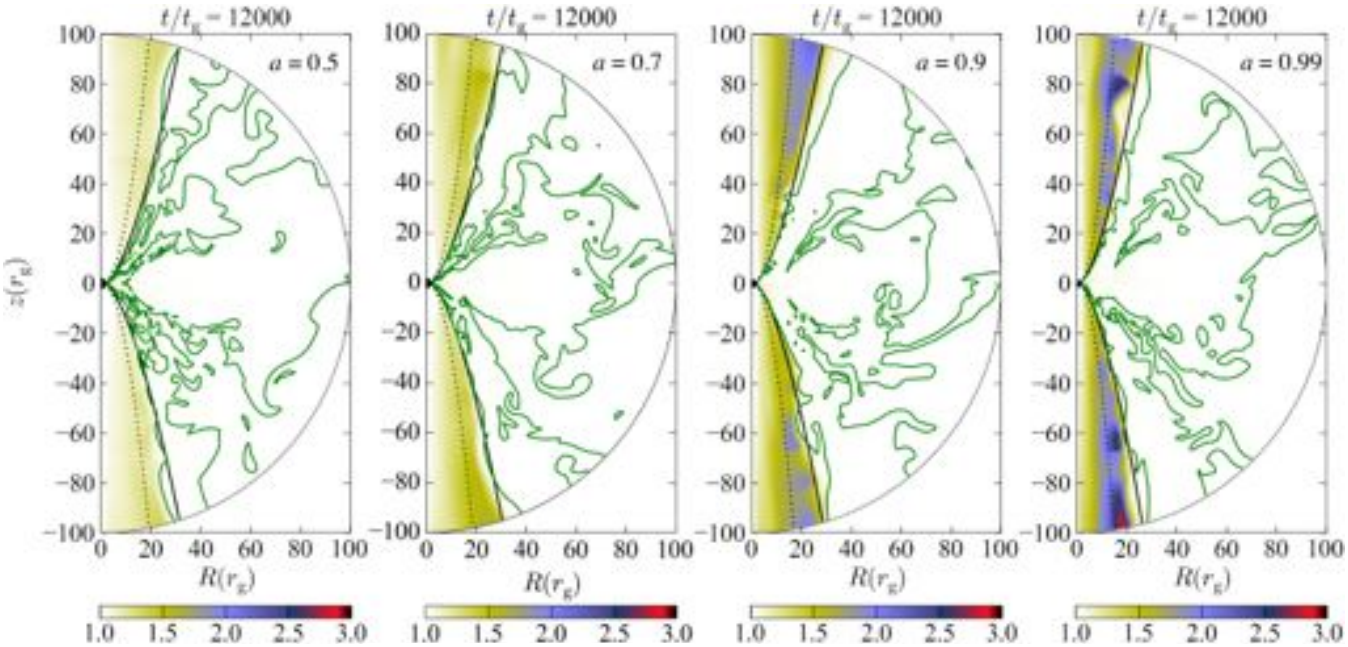

FIG. 12.— A color filled contour of the Lorentz factor Γ (only where $u^r > 0$) for four different runs with different black hole spins (from *left* to *right*: $a = 0.5$, 0.7, 0.9, and 0.99). The final snapshot ($t/t_g = 12000$) is displayed for each run with the whole computational domain $r/r_g \leq 100$ and $0 \leq \theta \leq \pi$. Green solid lines show $\beta_p = 1$ (in the fluid frame). Other components in panels are identical to those in Figure 8.

where

$$g_{tt} \equiv -(\Delta - a^2 \sin^2\theta)/\Sigma,$$
$$\Delta \equiv r^2 - 2r + a^2,\ \Sigma \equiv r^2 + a^2\cos^2\theta.$$

We report another visible dependence on the black hole spin a during the time evolution of the system in Figure 12, which exhibits Γ at the final stage $t/t_{\rm g} = 12000$, corresponding to each panel of Figure 8. It is notable that a high value of Γ ($\lesssim 1.5$ in $a = 0.7$, $\lesssim 2.3$ in $a = 0.9$, and $\lesssim 2.8$ in $a = 0.99$, respectively) is distributed between two outermost streamlines ($z \propto R^2$ and $z \propto R^{1.6}$) of the semi-analytical FFE jet, which are anchored to the horizon (Figure 1).

Qualitatively similar results (Γ becomes large at the outer layer in the funnel, while $\Gamma \simeq 1$ is sustained at the inner layer) are obtained in SRMHD simulations with a fixed jet boundary and a solid-body rotation at the jet inlet, which provides a good approximation of the behavior of field lines that thread the horizon (Komissarov et al. 2007, 2009). Furthermore, the trend can be seen in FFE ($a = 1$; Tchekhovskoy et al. 2008), GRFFE ($a = 0.9$–0.99; Tchekhovskoy et al. 2010), and GRMHD ($a = 0.7$–0.98; Penna et al. 2013) simulations with modified initial field geometries in the torus (Narayan et al. 2012). Note that the inner "cylinder-like" layer with a lower $\Gamma < 1.5$ for all spins arises from a suppression of the magnetic nozzle effect; an effective bunching poloidal flux takes place near the polar axis due to the hoop stresses (see Figure 9) so that enough separation between neighboring poloidal field lines is suppressed (see also Komissarov et al. 2007, 2009).

Another notable feature is the inhomogeneous distribution of Γ (blobs) at the outer layer in the funnel; throughout the time evolution, knotty structures are formed with $\Gamma \gtrsim 2$ when $a \geq 0.9$ (two *right* panels in Figure 12). Blobs appear at around the funnel edge $R/r_{\rm g} \gtrsim 10$ ($z/r_{\rm g} \gtrsim 20$) with $\Gamma \gtrsim 1.5$, which could be observed as a superluminal motion $\gtrsim c$ with a viewing angle $\lesssim 25^\circ$. Note that no proper motion has been detected within a scale of $100\,r_{\rm g}$ in de-projection in M87, where we interpret VLBI cores as an innermost jet emission. We discuss the formation of blobs and their observational counterparts in Section 5.3.2.

An evolution of the Lorentz factor in a highly magnetized MHD/FFE outflow can be expressed with the approximated formula (in the so-called "linear acceleration" regime[6]):

$$\Gamma \approx \sqrt{1 + (R\Omega)^2} \approx R\Omega \propto z^{1/\epsilon}, \quad (6)$$

where

$$\Omega \approx 0.5\Omega_{\rm H}(a). \quad (7)$$

$\Omega_{\rm H}$ denotes the angular frequency of the black hole event horizon as

$$\Omega_{\rm H}(a) = \frac{ac}{2r_{\rm H}}. \quad (8)$$

This formula is valid at a moderately relativistic regime $\Gamma \gtrsim 2$ (McKinney & Narayan 2007b; Komissarov et al. 2007, 2009, NMF07, TMN08) and/or all the way out to large distances (the jet radius is large enough: $R\Omega \gg 1$ where the curvature of the magnetic surface is unimportant; Beskin & Nokhrina 2006, 2009). This can be expected at $z/r_{\rm g} \gtrsim 100$ as is exhibited in the steady axisymmetric GRMHD solution (Pu et al. 2015). Numerical simulations of the FFE jets in both genuine parabolic and the BP82-type parabolic shapes provide a quantitative agreement with the analytical solution (TMN08).

Based on our result shown in Figure 12, at least up to $r/r_{\rm g} = 100$, we could not find clear evidence of linear acceleration in the funnel jet. This is presumably due to a lack of a differential bunching/collimation of the poloidal magnetic flux as is expected in a highly magnetized MHD/FFE regime (e.g. Tchekhovskoy et al. 2009) during the lateral extension of the funnel (in the regime of $R\Omega \gg 1$). However, there are visible increases of distributed Γ in the funnel jet as a increases. We can identify a physical reason in Figure 13; a concentration of the poloidal magnetic field becomes strong as r increases, but it is also enhanced as a function of a ($a = 0.5 \rightarrow 0.99$). As consequence of the differential operation of the magnetic nozzle effect, a larger Γ value in the funnel jet is obtained in the higher spin case. Note that blobs (knotty structures) also appear near the funnel boundary at $a \geq 0.9$ and we discuss this feature in Section 5.3.2.

Contours of the equipartition $\beta_{\rm p} = 1$ are also displayed in Figure 12. We can see that one of contours is elongated near the outermost BP82-type parabolic streamline. Thus, our boundary condition of the funnel edge (Equation 4) is moderately sustained up to $r_{\rm out}/r_{\rm g} = 100$ (there is a departure of $\beta_{\rm p} = 1$ from the funnel edge in $a = 0.9$, but this seems to be a temporal and/or boundary issue). Figure 12 also provides a clue of the velocity in the corona/wind region. At the funnel exterior, no coherent poloidal magnetic flux exists in the quasi-steady SANE state (Figure 9). The weakly magnetized ($b^2/\rho \ll 1$, $\beta_{\rm p} \simeq 1$) coronal wind carries a substantial mass flux compared with the funnel jet (Figure 11, see also Sadowski et al. 2013; Yuan et al. 2015). Therefore it is unlikely that the coronal wind could obtain a relativistic velocity; $\Gamma = 1$ is sustained in all cases with $a = 0.5$–0.99 (see also Yuan et al. 2015, with $a = 0$). Note that similar results are confirmed even in 3D simulations of the MAD state (e.g. Penna et al. 2013), in which the coherent poloidal magnetic flux is presumably arrested on the equatorial plane at $R > r_{\rm H}$ (Tchekhovskoy 2015).

With standard parameters in HARM, our GRMHD simulations provide several interesting results, which does not depend on the black hole spin when $a = 0.5$-0.99. We, however, need further investigations to find features such as a linear acceleration of the underlying flow with an extended computational domain ($r_{\rm out}/r_{\rm g} > 100$). Also, one of the important issues is to investigate whether an unbound wind could surely exist on large scales. If so, it indicates that $Be \simeq 0$ ($-u_t \simeq 1$) will not hold at the jet/wind boundary. How the BP82-type parabolic funnel jet could be maintained by an unbound wind and/or other external medium? How the equipartition conditions $b^2/\rho \simeq 0.5$–1 and $\beta_{\rm p} \simeq 1$ are maintained (or modified)? These questions will be addressed in a forthcoming paper.

3.2.3. *Jet Stagnation Surface*

We present Figure 14 to examine the jet stagnation surface and the local value of b^2/ρ, with respect to the black hole spin (a). As is also shown in Figure 11, the jet stagnation surface ($u^r = 0$ inside the funnel) shifts toward the black hole if a increases (see, e.g. Takahashi et al. 1990, for an analytical examination in the Kerr space-time) due to an increase of Ω

[6] In a less-collimated parabolic stream with $1 < \epsilon < 2$, an outflow also follows the so-called "power-law acceleration" regime, which exhibits a slower growth of $\Gamma \approx \sqrt{3/(\epsilon-1)}(\epsilon/\theta) \propto z^{(\epsilon-1)/\epsilon}$ than the linear acceleration (see TMN08; Komissarov et al. 2009, for details). A transition (from linear to power-law acceleration) depends on $\epsilon = 2/(2-\kappa)$ and $\theta_{\rm fp}$ (the colatitude angle at the footpoint; i.e., the event horizon in this paper).

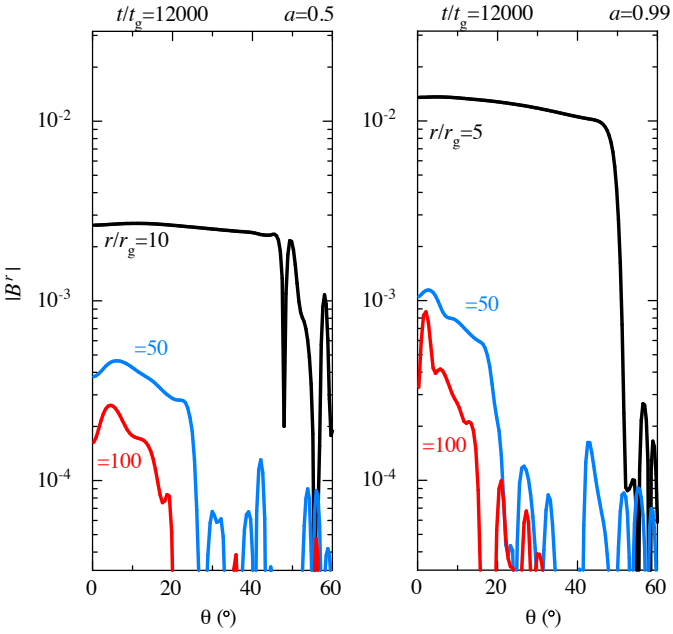

FIG. 13.— A θ cross-section at $r/r_{\rm g}$ =10 (black, *left*) or 5 (black, *right*), 50 (blue), and 100 (red) showing the absolute value of the radial magnetic field $|B^r|$ at $t/t_{\rm g} = 12000$; $a = 0.5$ (*left*) and $a = 0.99$ (*right*).

(the outflow can be initiated at the inner side), but qualitatively similar structures of the surface are obtained ($a = 0.5$–0.99) as is clearly seen in Figure 14.

Coherent poloidal magnetic field lines are regularly distributed inside the funnel edge along the outermost parabolic streamline (BP82: $z \propto r^{1.6}$), which is anchored to the event horizon. As the black hole spin increases, the density of contours becomes high, indicating that the poloidal field strength goes up. Especially, as is examined in Figure 3, it is prominent at around the polar axis (z) in the very vicinity of the event horizon ($r/r_{\rm g} \lesssim$ a few) as $a \to 1$ (e.g. Tchekhovskoy et al. 2010). The closest part (to the black hole) of the jet stagnation is located at around the funnel edge with $a = 0.5$–0.99. During the quasi-steady state, the jet stagnation surface is almost stationary in our GRMHD simulations. Outer edges of the stagnation surface in funnel jets ($r/r_{\rm g} \simeq$ 5–10 in the case of $a = 0.5$–0.99) give an (initial) jet half opening angle of $\sim 40°$–$50°$ in de-projection (see Figure 13 and 14).

Contours of b^2/ρ with selected values are also displayed on each panel of Figure 14 for our reference. In the vicinity of the black hole at $r/r_{\rm g} \lesssim 20$, the value of b^2/ρ decreases monotonically (approximately independent on the colatitude angle θ inside the funnel) as r increases. Again, this can be interpreted as a consequence of no visible (but very weak) bunching of poloidal magnetic flux at $r/r_{\rm g} \simeq$ 5–10 (around the stagnation surface edges in the case of $a = 0.5$–0.99), as is shown in Figures 4, 13, and 14. Thus, we may not expect a significant concentration of the mass density toward the polar axis at a few $\lesssim r/r_{\rm g} \lesssim 20$ as examined with our fiducial run in Section 3.1 (see also Figures 2 and 3). Depending on the black hole spin ($a = 0.5, 0.7, 0.9$ and 0.99), $b^2/\rho \simeq 2, 5, 10$ and 20 are identified at around the closest part (near the funnel edge) on the jet stagnation surface. This is located between two outermost streamlines ($z \propto r^2$ and $z \propto r^{1.6}$) of the semi-analytical solution of the FFE jet.

As is seen in Figure 12, a high value of Γ is distributed throughout an outer layer of the funnel between two outermost streamlines ($z \propto R^2$ and $z \propto R^{1.6}$), which are anchored to the event horizon. Having a high value of b^2/ρ at the jet launching point is suggestive that the flow will undergo bulk acceleration to relativistic velocities, as seen in Equation (1). This is a necessary, but not sufficient condition, as the magnetic nozzle effect is also needed, which can be triggered by a differential bunching of poloidal flux toward the polar axis. As is suggested in Takahashi et al. (1990); Pu et al. (2015), the location of the jet stagnation surface, where the magneto-centrifugal force is balanced by the gravity of the black hole, is independent of the flow property, such as the rate of mass loading, because it is solely determined by a and Ω (Equation 7). We point out that a departure of the jet stagnation surface from the black hole at a higher colatitude ($\theta \to 0$) gives a prospective reason for the lateral stratification of Γ at large distances (where the sufficient condition for the bulk acceleration may be applied).

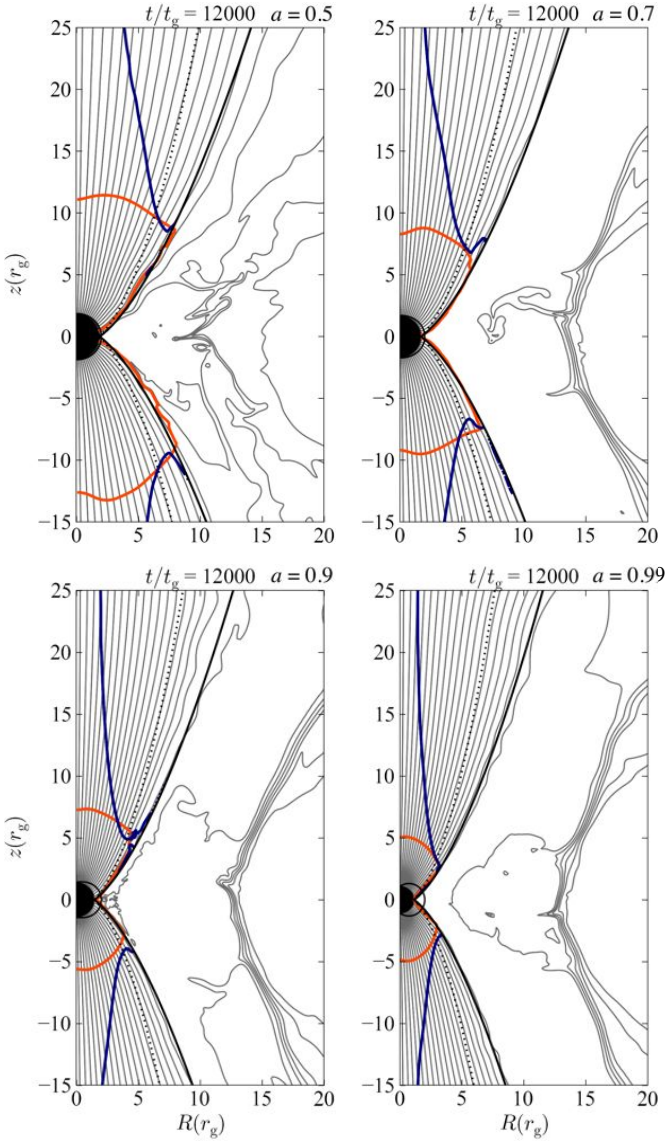

FIG. 14.— Similar to Figure 9, but the magnified view is shown for displaying the poloidal magnetic field line around the black hole with the computational domain $0 \le R/r_{\rm g} \le 20$ and $-15 \le z/r_{\rm g} \le 25$. The jet stagnation surface: $u^r = 0$ is drawn with navy solid lines on each panel (from *upper-left* to *lower-right*; different black hole spins of $a = 0.5, 0.7, 0.9$ and 0.99, respectively). Orange solid lines on each panel show i) $b^2/\rho = 2, 5, 10$, and 20, respectively (both at $z \lesseqgtr 0$).

The above issue could be associated with the so-called limb-brightened feature in the M87 jet. Note we identified the value of $b^2/\rho \simeq 0.5$–1 as the physical boundary at the funnel edge along the outermost BP82-type parabolic streamline, which is anchored to the event horizon. Thus, if this boundary condition holds even further downstream ($r/r_{\rm g} \gg 100$), the funnel edge is unlikely to be a site exhibiting a relativistic flow, as is examined in Figure 12. A highly Doppler boosted emission may not be expected there, but an alternative process, such as the in situ particle acceleration may be considered at the edge of the jet sheath (as a boundary shear layer) under the energy equipartition between the relativistic particles and the magnetic field (e.g. Stawarz & Ostrowski 2002). On the other hand, limbs in the M87 jet have a finite width δR inside their edges and δR seems to increase in the downstream direction (e.g. Asada et al. 2016), suggesting a differential bunching of streamlines (e.g. Komissarov 2011).

In this paper, we identify the outer jet structure (limbs) as the jet sheath, while the inner jet structure (inside limbs) is identified as the jet spine. In the next section, our results are compared with VLBI observations, followed by related discussions in Section 5. Especially, we assign Section 5.2 for discussion of a limb-brightened feature in the context of MHD jets and Section 5.3.2 to describe the origin of knotty structures.

4. COMPARISON WITH VLBI OBSERVATIONS

4.1. *Jet Morphology*

Figure 15 overviews the geometry of the M87 jet by compiling the data in the literature (see the caption for references). Multi-wavelength observations by Asada & Nakamura (2012, hereafter AN12) revealed that the global structure of the jet sheath is characterized by the parabolic stream $z \propto R^{1.73}$ at $z/r_{\rm g} \sim 400$–4×10^5 (see also Hada et al. 2013), while it changes into the conical stream $z \propto R^{0.96}$ beyond the Bondi radius of $r_{\rm B}/r_{\rm g} \simeq 6.9\times10^5$ (~ 205 pc: Rafferty et al. 2006). Hada et al. (2013) and Nakamura & Asada (2013) examined the innermost jet region ($z/r_{\rm g} \gtrsim 10$) by utilizing the VLBI core shift (Hada et al. 2011). Hada et al. (2013) which suggests a possible structural change toward upstream at around $z/r_{\rm g} \sim 300$, where the VLBA core at 5 GHz is located. The innermost jet sheath ($z/r_{\rm g} \gtrsim 200$) is recently revealed with HSA 86 GHz (Hada et al. 2016). Based on our theoretical examinations presented in previous sections, we overlay the outermost streamlines of the semi-analytical FFE jet model (NMF07, TMN08) with varying Kerr parameters ($a = 0.5$–0.99) on data points in Figure 15 for comparison.

There are notable findings: i) the inner jet radius (at $z/r_{\rm g} \lesssim 100$), which is represented by VLBI cores at 15–230 GHz, are traced by either outer parabolic or inner genuine parabolic streamlines of FFE jets, which are anchored to $r = r_{\rm H}$ with $\theta_{\rm fp} = \pi/2$. Within the uncertainties, we cannot distinguish the shape of the streamline, but there is a tendency that the mean values shift towards the genuine parabolic streamlines inside the funnel. Therefore, we consider that the mm VLBI core at 230 GHz with EHT observations (Doeleman et al. 2012; Akiyama et al. 2015, hereafter the EHT core) presumably show the innermost jet to be in a highly magnetized (PFD) regime $b^2/\rho \gg 1$ and $\Gamma \lesssim 1.5$ (see, Figures 8 and 12) inside the funnel. Note that the dominant magnetic energy of the VLBI core at 230 GHz is originally proposed by Kino et al. (2015). This may reflect the jet spine, however, rather than the jet sheath at the funnel edge (see Section 5.3.1 for discussions).

ii) At the scale of $100 \lesssim z/r_{\rm g} \lesssim 10^4$, we identify a clear coincidence between the radius of the jet sheath and the outermost BP82-type streamline of the FFE jet solution. We also confirm a reasonable overlap between the VLBI cores at 5 and 8 GHz and an extended emission of the jet sheath at VLBA 43 and HSA 86 GHz (see also Hada et al. 2013). Therefore, the hypothesis of the VLBI core as the innermost jet emission (Blandford & Königl 1979) is presumably correct at this scale although a highly magnetized state of VLBI cores, suggested by Kino et al. (2014, 2015) and the frequency (ν) dependent VLBI core shift $\Delta z(\nu) \propto 1/\nu$, taking place in the non-conical jet geometry in M87 (Hada et al. 2011) may conflict with original ideas in Blandford & Königl (1979, where an equipartition between the magnetic and synchrotron particle energy densities and a constant opening angle and constant velocity jet is considered). We also remind readers about our recent result on the jet geometry of blazars which examined VLBI cores (Algaba et al. 2017), suggesting that non-conical structures may exist inside the sphere of influence (SOI) $r_{\rm SOI} \sim 10^5$–$10^6\,r_{\rm g}$.

iii) At around $z/r_{\rm g} \simeq 10^4$–10^5, it is visible that data points (the radius of the jet sheath) start to deviate slightly from $z \propto R^{1.6}$, but a parabolic shape is sustained. This may indicate a new establishment of the lateral force-equilibrium between the funnel edge and the outer medium (wind/corona above the RIAF), *or* the jet sheath starts to be Doppler de-boosted (see Figures 16 and 18 as well as our discussion in Section 5.2). Previous GRMHD simulations exhibit a conical shape of the funnel edge at $z/r_{\rm g} \gtrsim$ a few of 100 (e.g. McKinney 2006), implying the jet is over-pressured against the outer medium. This however could not be the case in M87. The intrinsic half opening angle ($\theta_{\rm j}$) of the jet sheath attains the level of $\theta_{\rm j} \simeq 0.5^\circ$ at around $z/r_{\rm g} \simeq 4\times10^5$.

iv) Data points are clearly deviated from the outermost BP82-type parabolic streamlines of the FFE jet solution beyond $r_{\rm B}$. As is originally suggested by Cheung et al. (2007), a structured complex known as "HST-1" (Biretta et al. 1999) is located just downstream of $r_{\rm B}$ at around $10^6\,r_{\rm g}$. AN12 suggest a geometrical transition of the M87 jet as a consequence of the over-collimation of the highly magnetized jet at the HST-1 complex, which can be initiated by forming the HST-1 complex, at $\simeq r_{\rm B}$. The jet exhibits the conical geometry with $\theta_{\rm j} \simeq 0.5^\circ$ (const) at the kpc scale ($z/r_{\rm g} \gtrsim 3\times10^6$), while $\theta_{\rm j} \simeq 0.1^\circ$ is obtained at around HST-1. We can refer to another sample of the AGN jet structural transition at $\simeq r_{\rm SOI}$ in NGC 6251 (Tseng et al. 2016, see also Section 5.1).

Note the magnetic pressures at HST-1 and several knots in the downstream ($\simeq 10^{-9}$–10^{-8} dyn cm^{-2}; Owen et al. 1989; Perlman et al. 2003; Harris et al. 2009) are highly over-pressured against the ISM pressure of $\simeq 10^{-11}$–10^{-10} dyn cm^{-2} (Matsushita et al. 2002). Thus, the lateral pressure equilibrium between the conical jet sheath and the ambient medium does not seem to be sustained beyond $r_{\rm B}$. The inner part of highly magnetized jets can be heavily over-pressured with respect to the outer part due to the hoop stress as is examined in numerical simulations and self-similar steady solutions (Nakamura et al. 2006; Zakamska et al. 2008). A conical expansion of the highly magnetized (with a dominant toroidal field component), over-pressured jet sheath against the uniform ISM environment is reproduced in numerical simulations (e.g. Clarke et al. 1986).

As a summary of this section, we conclude that the edge of

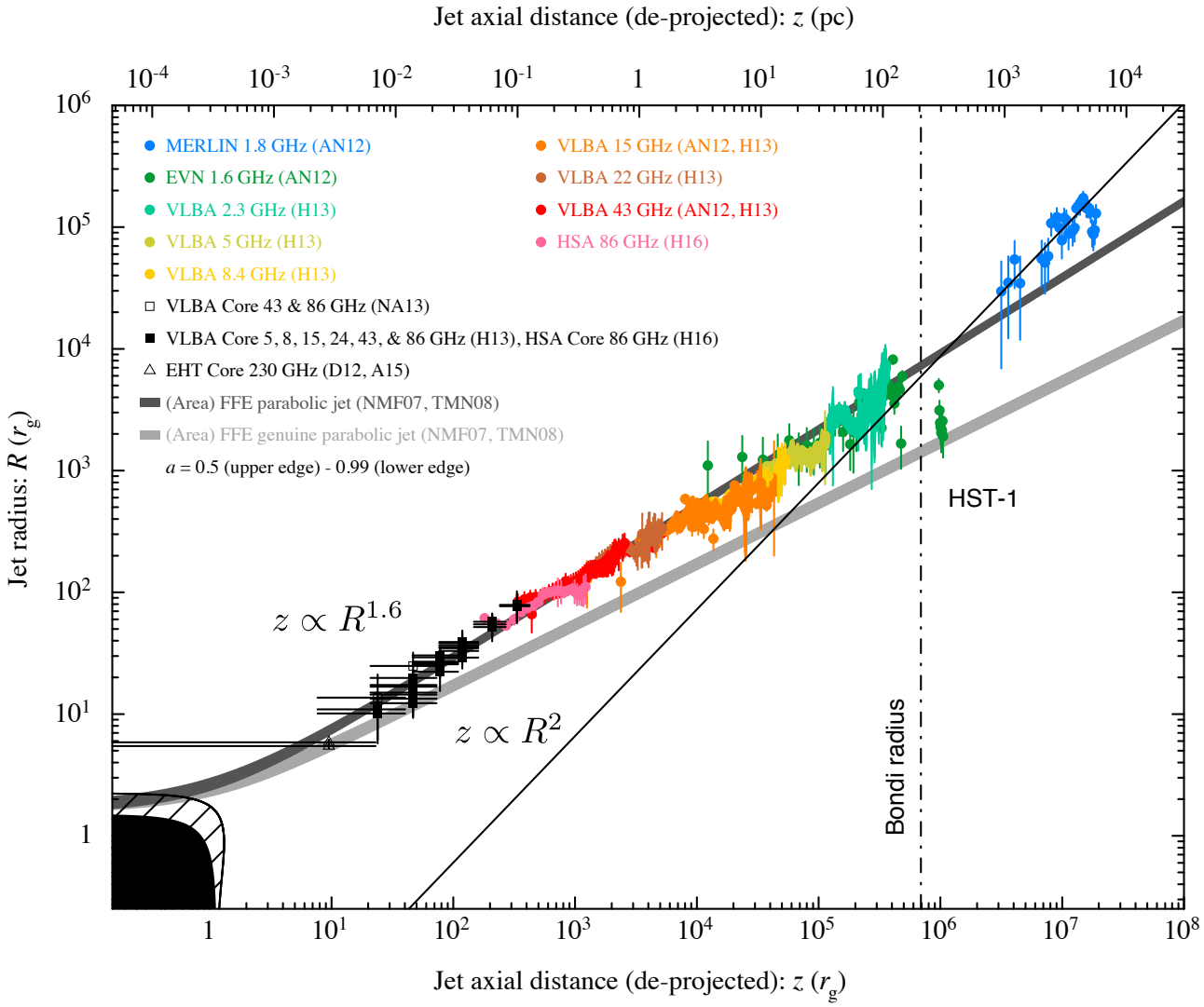

FIG. 15.— Distribution of the jet radius R as a function of the jet axial distance z (de-projected with $M = 6.2 \times 10^9 M_\odot$ and $\theta_v = 14°$) from the SMBH in units of r_g (cf. Asada & Nakamura 2012; Nakamura & Asada 2013; Hada et al. 2013, labeled as AN12, NA13, and H13, respectively). Additional data points are taken from Doeleman et al. (2012); Akiyama et al. (2015); Hada et al. (2016) (labeled as D12, A15, and H16, respectively). The (vertical) dashed-dotted line denotes the Bondi radius r_B, located at $\simeq 6.9 \times 10^5\, r_g$ and the HST-1 complex is around $10^6\, r_g$. Filled black region denotes the black hole (inside the event horizon), while the hatched area represents the ergosphere for the spin parameter $a = 0.99$. The light gray area denotes the approximate solution (e.g. NMF07, TMN08) of the FFE genuine parabolic jet (outermost BZ77-type streamline: $z \propto R^2$ at $R/r_g \gg 1$), while the dark gray area is the case of the parabolic jet (outermost BP82-type streamline: $z \propto R^{1.6}$ at $R/r_g \gg 1$), respectively. In both of the outermost streamlines, which are anchored to the event horizon with $\theta_{fp} = \pi/2$, a variation from $a = 0.5$ (upper edge) to $a = 0.99$ (lower edge) is represented as a shaded area. The solid line is the linear least-square for data points of MERLIN 1.8 GHz, indicating the conical stream $z \propto R$ (Asada & Nakamura 2012).

the jet sheath in M87 upstream of r_B can be approximately described as the outermost BP82-type streamline of the FFE jet solution with the Kerr parameter $a > 0$, which is anchored to the event horizon. Thus, we suggest the parabolic jet sheath in M87 is likely powered by the spinning black hole. Recent theoretical arguments clarified that the outward Poynting flux is generally non-zero (i.e., the BZ77 process generally works) along open magnetic field lines threading the ergosphere (Toma & Takahara 2014; Komissarov 2004). Thus our findings support the existence of the ergosphere. We note, however, that there is an alternative suggestion that the jet sheath is launched in the inner part of the Keplerian disk at $R \sim 10\, r_g$ (Mertens et al. 2016).

4.2. *Jet Kinematics*

Figure 16 overviews the jet kinematics by compiling the data in the literature (see the caption for references). Multi-wavelength VLBI and optical observations reveal both subluminal and superluminal features in proper motion, providing a global distribution of the jet velocity field V in M87. We display the value of $\Gamma\beta$ in Figure 16 by using simple algebraic formulas with the bulk Lorentz factor $\Gamma \equiv (1-\beta^2)^{-1/2}$ and $\beta = \beta_{app}/(\beta_{app}\cos\theta_v + \sin\theta_v)$, where $\beta = V/c$, and β_{app} is the apparent speed of the moving component in units of c, respectively. The value of $\Gamma\beta$ approaches β in the non-relativistic regime ($\Gamma \to 1$) and represents Γ in the relativistic regime ($\beta \to 1$), thereby representing simultaneously the full dynamic range in velocity over both regimes.

Superluminal motions ($\beta_{app} > 1$) have been frequently observed at relatively large distances beyond r_B. Furthermore, these components seem to originate at the location HST-1

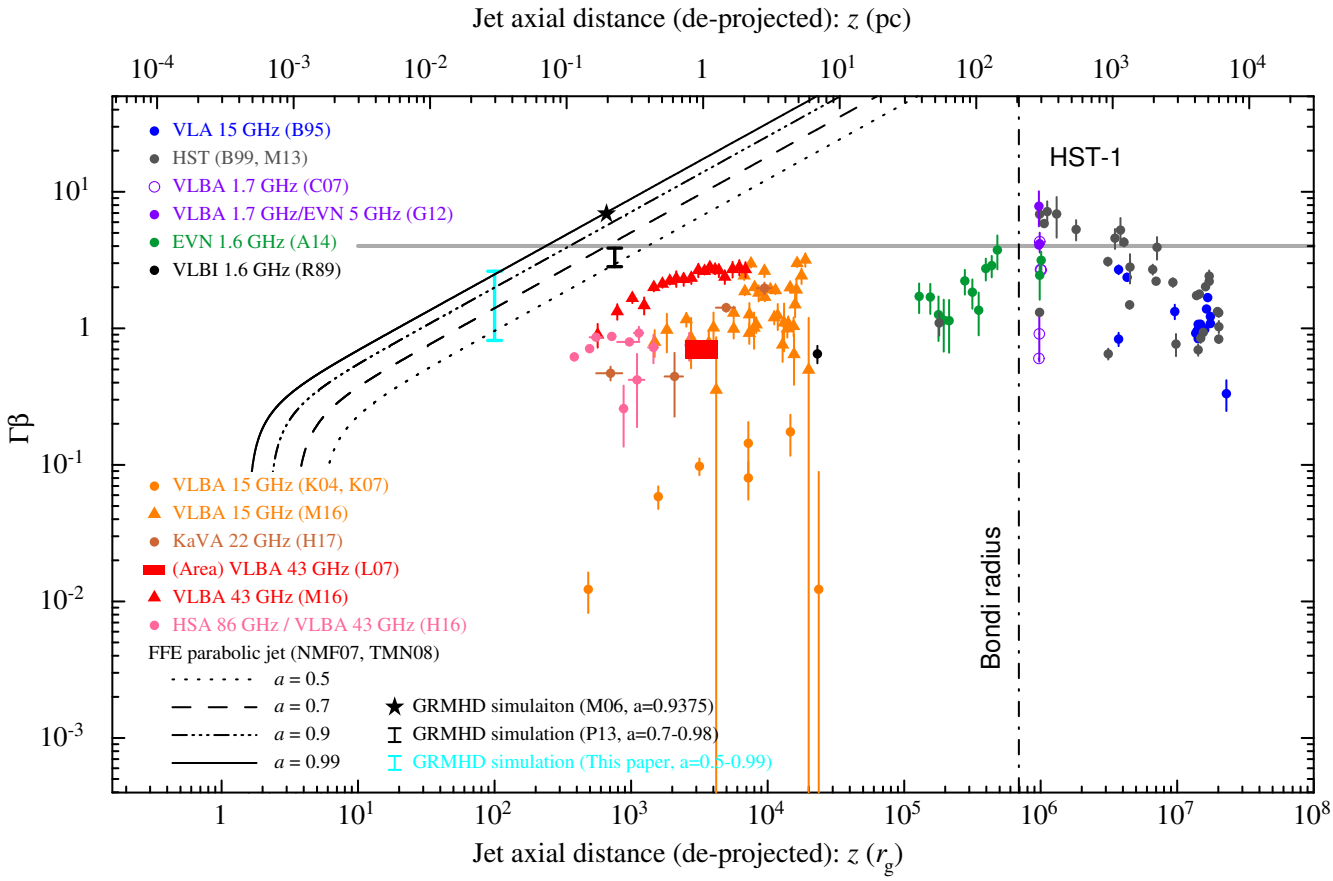

FIG. 16.— Distribution of $\Gamma\beta$ as a function of the jet axial distance z (de-projected with $M = 6.2 \times 10^9 M_\odot$ and $\theta_v = 14°$) from the SMBH in units of r_g. The data of proper motions is taken from the literature (Reid et al. 1989; Biretta et al. 1995; Biretta et al. 1999; Kellermann et al. 2004; Kovalev et al. 2007; Ly et al. 2007; Cheung et al. 2007; Giroletti et al. 2012; Meyer et al. 2013; Asada et al. 2014; Hada et al. 2016; Mertens et al. 2016; Hada et al. 2017, labeled as R89, B95, B99, K04, K07, L07, C07, G12, M13, A14, H16, M16 and H17, respectively). Theoretical expectation by utilizing the FFE parabolic ($z \propto R^{1.8}$) jet solutions (NMF07, TMN08) is also displayed with varying Kerr parameters ($a = 0.5$: dotted line, $a = 0.7$: dashed line, $a = 0.9$: dashed-three dotted line, and $a = 0.99$: solid line, respectively). The vertical solid line with horizontal bars (cyan) indicates a range of maximum values in the jet sheath (between two outermost streamlines; $z \propto R^2$ and $z \propto R^{1.6}$), which are obtained in our GRMHD simulations at around $r_{\rm out} = 100\, r_g$ ($a = 0.5$–0.99, see Figure 12). For our reference, the maximum value in McKinney (2006, labeled as M06) with $a = 0.9375$ is marked with a filled star. Also, the vertical solid line with horizontal bars (black) indicates a range of maximum values in Penna et al. (2013, labeled as P13) with $a = 0.7$–0.98. The horizontal gray line corresponds to $\Gamma\beta$ with $\beta = \cos\theta_v$, at which the Doppler beaming has a peak (see also Figure 18).

(Biretta et al. 1999; Cheung et al. 2007; Giroletti et al. 2012). On the other hand, no prominent superluminal features inside r_B have been confirmed in VLBI observations over decades (Reid et al. 1989; Kellermann et al. 2004; Ly et al. 2007). Instead, sub-luminal features are considered as non-bulk motions, such as growing instability patterns and/or standing shocks (e.g. Kovalev et al. 2007). Thus, this discrepancy (a gap between sub-luminal and superluminal motions along the jet axial distance) has been commonly recognized. Asada et al. (2014) discovered a series of superluminal components upstream of HST-1 ($z/r_g \sim 10^5$–10^6), providing the missing link in the jet kinematics of M87.

Very recently, superluminal motions on the scale of $z/r_g \simeq 10^3$–10^4 were finally discovered by Mertens et al. (2016); Hada et al. (2017). These observations give a diversity to the velocity picture, and suggests the hypothesis that the systematic bulk acceleration is taking place if the observed proper motions indeed represent the underlying bulk flow. A smooth acceleration from subliminal to superluminal motions upstream of HST-1 is argued in the context of the MHD jet with an expanding parabolic nozzle (Nakamura & Asada 2013; Asada et al. 2014; Mertens et al. 2016; Hada et al. 2017), while observed proper motions exhibit a systematic deceleration in the region downstream of HST-1 (Biretta et al. 1995; Biretta et al. 1999; Meyer et al. 2013) where the jet forms a conical stream.

Paired sub-/superluminal motions in optical/radio observations at HST-1 (Biretta et al. 1999; Cheung et al. 2007) (see Figure 16 at around $\sim 10^6\, r_g$) are modeled by the quad relativistic MHD shock system with a coherent helical magnetic field (Nakamura et al. 2010; Nakamura & Meier 2014). Taking the complex 3D kinematic features of trailing knots downstream of HST-1 (Meyer et al. 2013) into account, a growing current-driven helical kink instability associated with forward/reverse MHD shocks in the highly magnetized relativistic jet (Nakamura & Meier 2004) may be responsible for organizing the conical jet in M87 at kpc scale.

We examine here the jet kinematics with observations far upstream of HST-1 at $z/r_g \simeq 10^3$–10^4 (Kellermann et al. 2004; Kovalev et al. 2007; Hada et al. 2016, 2017; Mertens et al. 2016). The distribution of $\Gamma\beta$ reaches a maximum level of $\simeq 3$ and extends to a lower value by more than two orders of magnitude as is shown in Figure 16. Mertens et al. (2016) interpret that the flow consists of a slow, mildly

relativistic ($\Gamma\beta \sim 0.6$: sub-luminal) layer (the exterior of the jet sheath), associated either with instability patterns or winds, and a fast, relativistic ($\Gamma\beta \sim 2.3$: superluminal) layer (the jet sheath), which is an accelerating a cold MHD jet from the Keplerian disk (i.e., the BP mechanism). Note that $\beta_{\rm app} \simeq 1$ corresponds to $\Gamma\beta \simeq 1.46$ with $\theta_{\rm v} = 14^\circ$ in M87.

In our numerical results, maximum values of $\Gamma\beta \simeq 0.8$–2.6 [the solid cyan vertical line in Figure 16] is obtained at around $r_{\rm out}/r_{\rm g} = 100$ ($\theta \lesssim 10^\circ$), depending on the black hole spin. This range covers most of the higher part of observed proper motions. For sufficiently high spins ($a \geq 0.9$), bulk speeds of $\Gamma\beta \simeq 1.7$–2.6 could be associated with knotty structures (see, Figure 12). Thus, we give an additional interpretation that superluminal motions could be interpreted as moving blobs in the underlying flow of the jet sheath. Regarding highly sub-luminal motions, as is shown in Figures 11 and 12, we confirm a non-relativistic coronal wind universally exists for $a = 0.5$–0.99 with $\Gamma\beta \gtrsim 0.1$ (see also Yuan et al. 2015, for $a = 0$), which may be responsible for slow motions immediately exterior the jet sheath. An acceleration of winds is also of our interest, but it is unclear in our numerical results (see, Yuan et al. 2015, for their behaviors at $r/r_{\rm g} \gtrsim 100$).

Under the assumption that an observed moving component ($\beta_{\rm app}$) represents an underlying bulk flow (e.g. Lister et al. 2009), we compare observations with steady axisymmetric FFE jet solutions in Figure 16. $\Gamma\beta$ with Equation (6) is displayed with different black hole spins ($a = 0.5$–0.99). Our numerical simulations reveal that $b^2/\rho \simeq 0.5$-1 is sustained at the funnel edge along the outermost BP82-type parabolic streamlines of $z \propto R^{1.6}$. Therefore, significant acceleration through the FFE mechanism or magnetic field conversion is not expected here. Instead, the inner part of the funnel (the jet sheath/limb), where high ratio of magnetic to rest-mass energy density would be expected, is an appropriate region to apply the FFE jet solution. Parabolic streamlines of $z \propto R^{1.8}$ ($a = 0.5$–0.99) with $\theta_{\rm fp} = \pi/3$ are chosen as our reference solutions, taking into account that a peak in Γ lies asymptotically between two outermost streamlines ($z \propto R^2$ and $z \propto R^{1.6}$ in Figure 12).

A linear acceleration of highly magnetized MHD/FFE outflows can be expected in the moderately relativistic regime ($\Gamma \gtrsim 2$) with $\Gamma\beta \propto R \propto z^{0.56}$ ($\beta \to 1$) as is shown in Figure 16. Similar results are obtained by Beskin & Nokhrina (2006); McKinney & Narayan (2007b); Pu et al. (2015). Maximum values of $\Gamma\beta$ ($\simeq 0.8$–2.6) in our GRMHD simulations ($a = 0.5$–0.99) are qualitatively consistent with those of the FFE jet at $z/r_{\rm g} = 100$. We, however, consider this would be by coincidence as we cannot find any smooth increase in Γ well beyond ~ 2 within $r/r_{\rm g} = 100$ in Figure 12. FFE jet solutions with the parabolic shape of $z \propto R^{1.8}$ indicate $\Gamma\beta \sim 4$–30 around the scale of $z/r_{\rm g} \sim 10^3$–10^4 ($a \geq 0.5$). This velocity range corresponds to $\beta_{\rm app} \approx 4$–$8$ with $\theta_{\rm v} = 14^\circ$ in M87. There is a clear discrepancy between observed proper motions and theoretical expectations.

In reality, AGN jets at VLBI scale may not be exactly described by the FFE system. An agreement between the GRMHD results and FFE models is found to be good as far as $r/r_{\rm g} \sim 10^3$; beyond this scale the matter inertia becomes non-negligible ($\Gamma \gtrsim 10$) in GRMHD simulations (McKinney & Narayan 2007a). As a consequence, a slower evolution than $\Gamma\beta \propto R$ may presumably take place. Nonetheless, a departure from $\Gamma \sim 2$ at $z/r_{\rm g} \gtrsim 100$ could be expected in a GRMHD simulation if b^2/ρ is sufficiently large ($\gg 1$) at the jet stagnation surface. To be fair enough, $\Gamma\beta \lesssim 7$ is achieved at $z/r_{\rm g} \simeq 700$ in McKinney (2006)[7], which is quantitatively consistent with the FFE jet with $a = 0.9$–0.99 (see Figure 16). On the other hand, for a moderate case of $b^2/\rho \lesssim 100$, maximum values of $\Gamma\beta \simeq 3$–4 are reported at $z/r_{\rm g} \simeq 1000$ with $a = 0.7$–0.98 (Penna et al. 2013), indicating that a slower evolution is taking place than in highly magnetized GRMHD/FFE outflows (see also Figure 16).

As is mentioned above, the detection of faster proper motions $\beta_{\rm app} \gtrsim 4$ (~ 15 mas/yr) and a signature of their accelerations at $z/r_{\rm g} \sim 10^3$–10^4, where the jet sheath maintains a parabolic shape, will be key to confirming our GRMHD parabolic jet hypothesis. A VLBI program with 15/22/43 GHz towards M87 with a high-cadence monitoring of less than a week (conducting each observation every few days over a few weeks) may be feasible to find motions faster than $\gtrsim 0.3$ mas/week.

5. DISCUSSIONS

Topical issues are discussed for applying our results to other AGN jets and highlighting some future study on the M87 jet.

5.1. *Similarities between NGC 6251 and M87*

Tseng et al. (2016, hereafter T16) analyzed multi-frequency data (VLBA, EVN, and VLA) to investigate the jet structure in NGC 6251 and detect a structural transition of the jet radius from a parabolic to a conical shape at (2–4) $\times 10^5\, r_{\rm g}$, which is close to $r_{\rm SOI} \simeq 10^6\, r_{\rm g}$ in this source. This is a remarkably similar result to M87 (AN12); one may consider the virial equilibrium at the center of the cooling core in the giant elliptical galaxies as a thermodynamically stable state, which gives $r_{\rm B} \approx r_{\rm SOI}$. Furthermore, the jet radii (in units of $2r_{\rm g}$) before/after the transition are quantitatively overlapped with M87 as is shown in Figure 3 of T16. Obviously,

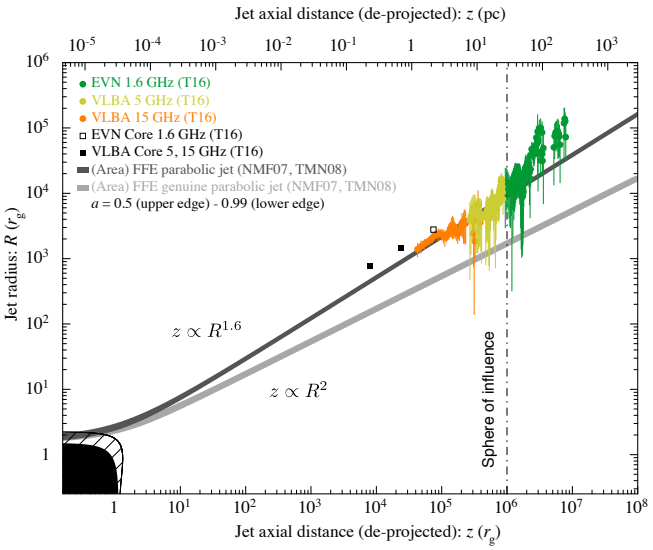

FIG. 17.— Distribution of the jet radius R in NGC6251 as a function of the jet axial distance z (de-projected with $M = 6 \times 10^8 M_\odot$ and $\theta_{\rm v} = 19^\circ$) from the SMBH in units of $r_{\rm g}$ (T16). This is similar to Figure 15; the vertical/horizontal scales and other components, which are shown in this figure, are identical.

[7] McKinney (2006) uses $a = 0.9375$ (the fiducial value), but a modified floor model is adopted; factors 10^{-7} in both power-law forms of $\rho_{\rm min}$ and $u_{\rm min}$ as well as a steep gradient of $r^{-2.7}$ in both cases. This ensures a huge value of $b^2/\rho \lesssim 10^7$ near the black hole in the PFD funnel.

this implies a tight correlation between the jet sheath and the outermost BP82-type parabolic streamline of the FFE jet solution as seen in M87 (Figure 15). Figure 17 confirms this at a quantitative level in NGC 6251.

T16 performed the broken power-law fitting and obtained $z \propto R^{2.0}$ at $\lesssim 4.2 \times 10^5\, r_{\rm g}$ and $z \propto R^{0.94}$ far beyond. We hereby suggest that the inner jet could be the BP82-type parabolic geometry, which is similar to M87 (Figure 17), if a position offset of VLBI cores from the SMBH $\simeq 8 \times 10^3\, r_{\rm g}$ in T16 is taken into account. Note that the radius of the EVN core at 1.6 GHz is almost identical to the radii of the VLBA jet at 15 GHz, as is shown in Figure 17 so we also confirm the VLBI core can be identified as the innermost jet emission given at these frequencies, which is also similar to M87 (Nakamura & Asada 2013; Hada et al. 2013). By comparing Figure 15 and Figure 17, we realize that the data points of M87 (inside $r_{\rm B}$) are distributed across more orders of magnitude than NGC 6251 (inside $r_{\rm SOI}$). Thus, VLBI observations at higher frequencies are needed to confirm a precise power-law index in the parabolic stream inside the SOI.

The difference of the SMBH mass between M87 and NGC 6251 is about one order of magnitude. If the jet radial and axial sizes are normalized in units of $r_{\rm g}$, they are remarkably identical (see, Figures 15 and 17 in this paper, and Figure 3 in T16). This suggests us the structural transition may be a characteristic of AGN jets, at least in nearby radio galaxies. It is straightforward to seek a counterpart by studying nearby blazars with a relatively large SMBH mass of $M \sim 10^9$–$10^{10}\, M_\odot$. Historically, the upstream region of conical jets in blazars (i.e., inside the VLBI cores at $\lesssim 0.1$ mas[8] at mm/cm wavelengths) has been unresolved. They are sometimes called the "pipe-line" from the central energy generator to the jet, which is unknown and even said that it may not exist (see, the schematic view: Marscher & Gear 1985). Therefore, we expect that ultra-high-angular-resolution VLBI at mm (HSA, GMVA, EHT) wavelengths with ALMA will explore the non-conical pipe-line inside $r_{\rm SOI}$ for bright nearby blazars.

5.2. *A Limb-brightened Feature in the M87 Jet*

A limb-brightened feature, one of the unanswered issues in the M87 jet, is discussed by Hada et al. (2016); according to the jet spine-sheath scenario by the presence of a velocity gradient transverse to the jet (e.g. Ghisellini et al. 2005; Clausen-Brown et al. 2013)[9], viewing the M87 jet from an angle $\theta_{\rm v} = 14°$ would not cause a limb-brightened feature unless the jet spine was unrealistically faster than the jet sheath, indicating alternative processes are involved (see, Hada et al. 2016, and references therein). Let us re-visit this issue based on Figure 16; a relativistic beaming effect in the M87 jet is diagnosed with the Doppler factor $\delta = \{\Gamma\,(1 - \beta\cos\theta_{\rm v})\}^{-1}$ on the scale of $z/r_{\rm g} \sim 10^3$–10^4, where β and Γ are adopted from observed proper motions and the MHD jet theory.

The observed synchrotron flux density S_ν for a relativistically moving component is enhanced by a beaming factor $\delta^{3-\alpha}$ (Jorstad et al. 2005; Savolainen et al. 2010), where

[8] Corresponding distances ~ 10 pc for FSRQs at $\langle z\rangle \sim 1.11$ and ~ 6 pc for BL Lacs at $\langle z\rangle \sim 0.37$ at an average redshift (e.g. Dermer 2007) with a viewing angle of 5° for our reference. Thus, the region $\lesssim 10^5\, r_{\rm g}$ for $M \gtrsim 10^9\, M_\odot$ has been unexplored in many blazars.

[9] The radio emission seen at a large viewing angle $\theta_{\rm v}$ is mostly coming from the slower sheath, while the emission from the faster spine is beaming away from the line of sight, because a Doppler factor as a function of $\beta(\equiv V/c)$ has a peak at $\beta = \cos\theta_{\rm v}$.

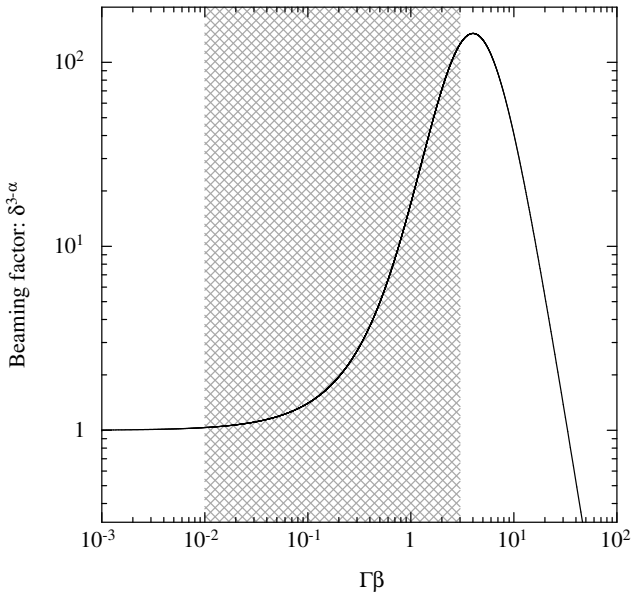

FIG. 18.— Distribution of the beaming factor $\delta^{3-\alpha}$ as a function of $\Gamma\beta$. $\theta_{\rm v} = 14°$ and $\alpha = -0.5$ are adopted. Cross-hatched gray area highlights the Doppler boosting with beaming factors of $\sim$ 1–100 at $10^{-2} \lesssim \Gamma\beta \lesssim 3$, corresponding to the observations at $z/r_{\rm g} \sim 10^3$–10^4 in Figure 16. Note that a peak of the curve is located at $\Gamma\beta$ with $\beta = \cos\theta_{\rm v}$.

α is the spectral index defined as $S_\nu \propto \nu^{+\alpha}$. We here adopt $\alpha = -0.5$ for the reference and the corresponding beaming factor is displayed as a function of the 4-velocity $\Gamma\beta$ in Figure 18. The beaming factor becomes less than unity in the highly relativistic regime $\Gamma\beta \gtrsim 30$. By taking into account the observed proper motions in HSA 86 GHz, VLBA 15/43 GHz, and KaVA 22 GHz on the scale of $z/r_{\rm g} \sim 10^3$–10^4, which corresponds to $\Gamma\beta \simeq 10^{-2}$–3 in Figure 16, the beaming factor is expected to be $\sim$ 1–100 at the jet sheath. Note that a similar range of beaming factors can be expected at $\Gamma\beta \simeq 4$–30, which is expected in the FFE jet solutions for the parabolic geometry ($z \propto R^{1.8}$) with $a = 0.5$–0.99 at $z/r_{\rm g} \sim 10^3$–10^4 in Figure 16.

As Equation (6) suggests, the linear acceleration of a highly magnetized MHD/FFE outflow decreases toward the polar region of the funnel when the power-law index of the parabola (ϵ) becomes large. A quasi-homogeneous distribution of the magnetization σ ($\approx b^2/\rho$) along the colatitude angle (θ) at $r/r_{\rm g} \lesssim 20$ and the structure of the jet stagnation surface, as is revealed in our GRMHD simulations (see Figure 14), may provide a feasible reasoning for an efficient bulk acceleration at the outer jet sheath, where the magnetic nozzle effect would be expected under the progress of a differential bunching of the poloidal magnetic flux toward the polar axis.

Therefore, the jet spine can be intrinsically less beamed than the jet sheath as the distribution of Γ exhibits (Figure 12; see also Tchekhovskoy et al. 2008, 2010; Penna et al. 2013). A lateral stratification of Γ is naturally expected so that a limb-brightened feature may be fundamental in AGN jets if they consist of black hole-driven GRMHD outflows. Interestingly, limb-brightened features are also observed in the best known TeV BL Lac objects Markarian (Mrk) 421 (Piner et al. 2010) and Mrk 501 (Giroletti et al. 2008; Piner et al. 2009) on $z/r_{\rm g} \simeq 10^4$–10^5 even with smaller angles of $\theta_{\rm v} = 4°$ (Giroletti et al. 2004; Lico et al. 2012).

Based on our numerical results up to $r_{\rm out}/r_{\rm g} = 100$, we find no relevant evidence of a concentration of the poloidal

magnetic flux at the funnel edge (Gracia et al. 2009) and/or a pileup of the material along the funnel edge (Zakamska et al. 2008), which might be related to a funnel-wall jet (De Villiers et al. 2003, 2005), as a possible mechanism of a limb-brightened feature. Note these may conflict with the physical conditions necessary to accelerate MHD jets, e.g., a high ratio of magnetic to rest-mass energy density and the magnetic nozzle effect. It would, however, be necessary to conduct a further investigation of this issue at the corresponding scale ($z/r_{\rm g} \gtrsim 10^3$).

We comment on the power-law acceleration (see the footnote 7) in the jet sheath (possibly, a less-collimated parabolic stream than the genuine parabolic one). As is shown in Figure 16, steady axisymmetric FFE jet solutions for streamlines of $z \propto R^{1.8}$ ($a = 0.5$–0.99) with $\theta_{\rm fp} = \pi/3$ (as the jet sheath) does *not* exhibit a transition from the linear to power-law acceleration at $z/r_{\rm g} < 10^5$ (it takes place at $z/r_{\rm g} > 10^{10}$ for $a = 0.99$). Thus, the outer jet sheath is always faster than the inner jet spine, even if the jet spine is launched with a sufficiently high value of b^2/ρ at the jet stagnation surface and Γ follows the linear acceleration due to an efficient magnetic nozzle effect. Both of these factors, however, are not supported by our GRMHD simulations. Therefore, we suggest the limb-brightened feature in M87 may be associated with the intrinsic property of an MHD parabolic jet powered by the spinning black hole, rather than the result of a special viewing angle as is previously discussed in (Hada et al. 2016).

Finally, as is mentioned in Section 4.1, the radius of the jet sheath starts to deviate slightly (becoming narrower) from the outermost BP82-type streamline $z \propto R^{1.6}$ at $z/r_{\rm g} \gtrsim 10^4$ (see also Figure 15). If the jet sheath follows the linear acceleration up to this scale, as is examined in Figure 16, the underlying flow would reach $\Gamma\beta \simeq 30$ ($a = 0.9$–0.99) and result in a weaker Doppler de-boosting (Figure 18). Furthermore, it is interesting to note that the emission of the parabolic jet sheath further downstream disappears at $z/r_{\rm g} \gtrsim 4 \times 10^5$ (Asada et al. 2014), where $\theta_{\rm j} \simeq 0.5^\circ$ is obtained (Figure 15). If the empirical relation $\Gamma\theta_{\rm j} \sim 0.1 - 0.2$ (Clausen-Brown et al. 2013) is applied, $\Gamma \simeq 11$–22 would be expected. This is close to the velocity range, at which a Doppler de-boosting may arise.

5.3. *VLBI Cores in M87*

We now discuss the (sub-)mm VLBI cores in M87, which are considered the innermost jet emission—at the given frequencies—in the vicinity of the SMBH (see also Figure 15). Figure 19 shows the radius and location of VLBI cores at mm bands (43, 86, and 230 GHz) and their expectation at sub-mm bands (345 and 690 GHz), by an extrapolation of the VLBI core at frequencies higher than 43 GHz (Hada et al. 2013; Nakamura & Asada 2013) and utilizing the frequency depending VLBI core shift (Blandford & Königl 1979) in M87 (Hada et al. 2011). Our GRMHD simulation result for $a = 0.9$ is overlaid for reference. What we currently know about the (sub-)mm VLBI cores of M87 from observations are the size, the flux density, the brightness temperature (Doeleman et al. 2012; Akiyama et al. 2015), and the energetics (Kino et al. 2014, 2015).

5.3.1. *(Sub-)mm VLBI Core as a Neighborhood of the Jet Origin*

The synchrotron self-absorption (SSA) theory is applied in order to examine the energy balance between electrons (U_e) and magnetic fields (U_B) for the VLBA core at 43 GHz; it can be highly magnetized or at most roughly in equipartition

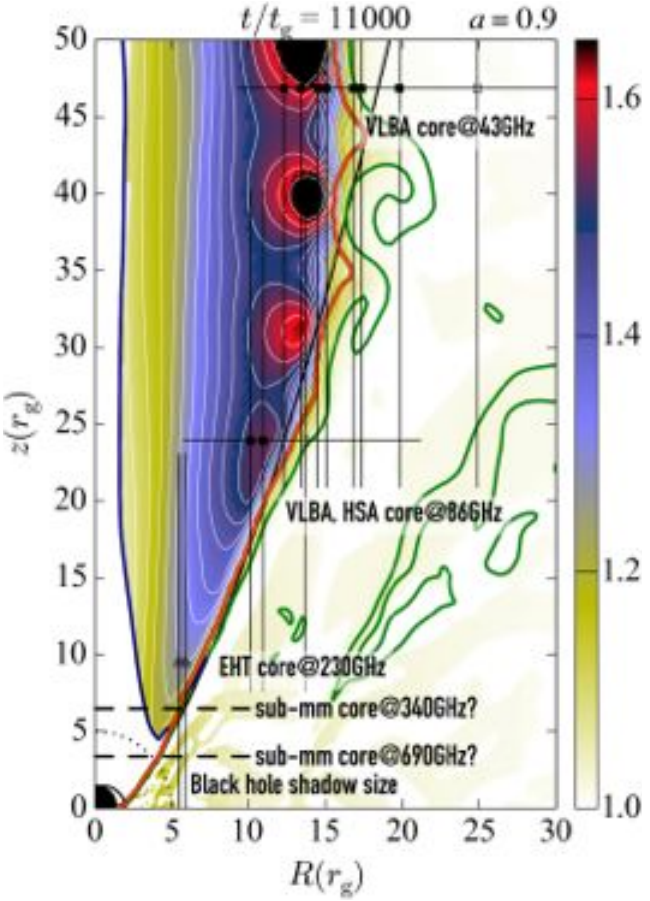

FIG. 19.— Innermost jet radii are displayed as the FWHM/2 of mm VLBI cores at 43, 86, and 230 GHz, by utilizing the VLBI core shift. Our GRMHD simulation result ($a = 0.9$) in the quasi-steady phase ($t/t_{\rm g} = 11000$) is overlaid. Expected positions of sub-mm VLBI cores at 345 and 690 GHz are also indicated with a horizontal dashed line. A color filled contour of the Lorentz factor Γ (only where $u^r > 0$) is shown as well as $\beta_{\rm p} = 1$ (green solid lines), the jet stagnation surface $u^r = 0$ (a navy solid line: only inside the PFD funnel), and $b^2/\rho = 1$ (an orange solid line). Other components are identical to those in Figure 1, but the black hole spin is adjusted. The size of the black hole shadow is indicated with the dotted circle with the average radius $\sim 5\,r_{\rm g}$ for our reference. See also Figures 5, 12, and 15 for details.

($10^{-4} \lesssim U_e/U_B \lesssim 0.5$; Kino et al. 2014). Furthermore, Kino et al. (2015) derived the energy balance of electrons and positrons ($U_\pm$) and U_B in the EHT core at 230 GHz as $8 \times 10^{-7} \leq U_\pm/U_B \leq 2 \times 10^{-3}$. These constraints, together with their locations ($R/r_{\rm g}$, $z/r_{\rm g}$) in the funnel, may provide some hint for how to discriminate between the (sub-)mm and mm cores as is shown in Figure 19.

Under the hypothesis that (sub-)mm VLBI cores consist of the optically thick (against SSA) non-thermal synchrotron emission from the innermost jet, mm VLBI core emission (≤ 86 GHz) may be dominated by the jet sheath close to the funnel edge ($b^2/\rho \simeq 1$ and $\beta_{\rm p} \simeq 1$). The (sub-)mm VLBI core emission (≥ 230 GHz) may be dominated by the jet spine further inside the funnel edge ($b^2/\rho \gg 1$ and $\beta_{\rm p} \ll 1$), though we may not rule out a possible contribution of the RIAF body ($b^2/\rho \ll 1$ and $\beta_{\rm p} \geq 1$) (Kino et al. 2015; Akiyama et al. 2015); the brightness temperature of $\sim (1-2) \times 10^{10}$ K of the EHT core is broadly consistent with the electron temperature of $\sim 10^9$–10^{10} K in the advection-dominated accretion flow (Mahadevan 1997).

Temporal variations of the FWHM size as well as the flux density of (sub-)mm VLBI cores (spanning from months to

years) may also provide another important clue for the local behavior of the jet as is shown in Figure 19. It is notable that the FWHM size of VLBI cores at 43/86 GHz is changing with variable flux density within a factor of ~ 2 (Nakamura & Asada 2013; Hada et al. 2013, 2016), while the EHT core at 230 GHz is fairly stable without a significant change of the flux density spanning three years (Akiyama et al. 2015). On the other hand, the light curve of the SMA data at 230 GHz appears to exhibit a monthly scale variation (Hada et al. 2014), implying that the variability may arise on the scale larger than $10\,r_{\rm g}$, which corresponds to the size of the jet radius ($\gtrsim$ a few tens of $r_{\rm g}$) where blobs emerge and propagate in our GRMHD simulations.

Thus, no significant variations of the FWHM size as well as the flux density spanning three years (Akiyama et al. 2015) and a theoretical constraint toward a highly magnetically dominated state (Kino et al. 2015) in the EHT core give us a favor that a emission comes form the innermost jet (inside the funnel) within $z/r_{\rm g} \lesssim 20$, whereas further multi-epoch observations would be desired to confirm our hypothesis. As is shown in Figure 19, position uncertainties of (sub-)mm VLBI cores allows us to consider either the jet and/or the RIAF as an emission source. Thus, polarization structures at (sub-)mm bands would be important to study the origin of the synchrotron emission of VLBI cores; either a toroidal component (from the RIAF and/or corona/wind) or a helical component (from the funnel). Furthermore, an existence of sub-mm VLBI cores at 345/690 GHz (or perhaps non-existence due to a truncation of the core emission beyond the jet stagnation surface) may provide a further constraint.

Figure 19 also indicates the FWHM/2 size of the EHT core $\simeq 5\,r_{\rm g} \sim 20\,\mu$as (Doeleman et al. 2012; Akiyama et al. 2015) at 230 GHz is comparable to a largest extent of the stagnation surface (i.e., a minimum extent of the funnel jet radius at the approaching side) for the BH spin $a \sim 0.9$. This is also similar size of the photon ring (i.e., the black hole shadow) with the average radius of $\sim 5r_{\rm g}$ (Chan et al. 2013). Therefore, the observed (sub-)mm VLBI core structure at 230 GHz (and above) may be affected by the photon ring and/or the gravitational lensing of surrounding emission (e.g. the RIAF, the counter jet, and so on). Our discussion does not consider this, while our results are not affected by this. We speculate that some prominent feature associated to the jet base, which can be connected to the spinning black hole with $\Omega_{\rm H}$, may be expected if the stagnation surface is the initiation site of the particle acceleration (e.g. Broderick & Tchekhovskoy 2015; Pu et al. 2017).

5.3.2. *Origin of Superluminal Blobs and Shock-in-jet Hypothesis*

Distribution of Γ in Figure 19 clearly exhibits an existence of the cylindrical core with $\Gamma \lesssim 1.2$ inside the funnel ($R/r_{\rm g} \lesssim 5$), accompanied with a lateral increase of Γ along the R-axis (see also Figure 12). The funnel jet does not exhibit a significant acceleration with remaining $\Gamma \lesssim 1.5$ at $z/r_{\rm g} \lesssim 50$, where it does not fully enter the linear acceleration regime ($R\Omega \gg 1$). Outside the funnel, the bound wind exists, but $\Gamma = 1$ is sustained. However, it is notable that there is an emergence of blobs with $\Gamma \gtrsim 1.5$ in the funnel jet (we confirmed similar events take place when $a \geq 0.7$).

We consider that a formation of high-Γ blobs in the underlying low-Γ bulk flow near the black hole may be a fundamental phenomena in the system, giving a physical origin of superluminal motions as seen in mm/cm VLBI observations (see Figure 16). A blob, which may be a compressional magnetosonic wave triggered by the axisymmetric distortion such as an $m = 0$ mode instability inside the funnel edge, could steepen into a magnetosonic shock. Therefore, moving a shock in the jet ("shock-in-jet", e.g. Blandford & Königl 1979; Marscher 1980) is presumably expected as a counterpart of enhanced synchrotron emission, especially at the jet sheath. Thus our GRMHD simulations provide a self-consistent process how superluminal blobs in AGNs could be originated in the vicinity of the SMBH.

This feature has never been seen in previous simulations with a fixed curvilinear boundary wall (Komissarov et al. 2007, 2009; Tchekhovskoy et al. 2008, 2010), implying a dynamical consequence of the external boundary during the evolution of PFD funnel jets. It seems that a blob appears beyond $R \simeq 10\,r_{\rm g} (> R_{\rm L})$ (where $R_{\rm L}$ is the outer light surface and $R_{\rm L} \sim 5$ for the case of $a = 0.9$, e.g. McKinney 2006; Pu et al. 2015) due to a lateral compression of the funnel-wall as is shown in Figure 19. Note that previous GRMHD simulations (McKinney 2006) also experience that, beyond $r \approx 10\,r_{\rm g}$, as the jet undergoes poloidal oscillations due to toroidal pinch instabilities; Γ is larger in pinched regions than non-pinched regions.

We suggest that the pressure driven (interchange) and/or the current driven instability, such as sausage/pinch mode (the azimuthal mode number: $m = 0$) may play a dynamical role. In the highly magnetized PFD funnel, the outer Alfvén surface is fairly close to the outer light surface, where the azimuthal component of the magnetic field is comparable to the poloidal one (McKinney 2006; Pu et al. 2015). The azimuthal component of the magnetic field becomes dominant in the super-Alfvénic flow and if the ratio of the toroidal to poloidal field strength becomes larger than $\sqrt{2}$, such an instability may take place (e.g. Kadomtsev 1966; Priest 1982). $\beta_{\rm p} \simeq 1$ is located just at the funnel edge (see also Figures 5, 12, and 19) and we thus consider that the $m = 0$ mode is excited at around the jet sheath at $R/r_{\rm g} \gtrsim 10$, but it could be suppressed at the inner jet spine and the vicinity of the black hole where $\beta_{\rm p} \ll 1$.

One of the good examples is provided by VLBI observations with the HSA at 86 GHz (Hada et al. 2016); we remark the axisymmetric "bottle-neck" structure at $\sim$ 0.2–0.3 mas ($\sim$ 230–340 $r_{\rm g}$ in de-projection) from the core. We further point out knot-like enhanced intensity features as an appearance of paired 'blobs' at both northern and southern limbs (labeled as N1/S1–N4/S4) up to ~ 1 mas ($\sim 10^3\,r_{\rm g}$) in Hada et al. (2016). Distribution of quasi-axisymmetric blobs (northern/southern limbs) extends up to ~ 10 mas ($\sim 10^4\,r_{\rm g}$), which is revealed by the VLBA at 43 GHz (Walker et al. 2018) and the KaVA at 23 GHz (Niinuma et al. 2014). Oscillatory patterns, most likely reflecting over-collimation/-expansion of the flow, are seen at $\lesssim 10$ mas scale of the jet sheath (Mertens et al. 2016).

The very high energy (VHE; > 100 GeV) γ-ray flares in M87 (see Abramowski et al. 2012, for an overview) may originate in the jet base within $\sim 100\,r_{\rm g}$, which is associated to the radio core at 43 GHz in 2008 (Acciari et al. 2009), 2010 (Hada et al. 2012), and 2012 (Hada et al. 2014). During an enhanced VHE γ-ray state in 2012, mm VLBI (EHT) observations of M87 at 230 GHz have been conducted. There is little possibility of the VHE γ-ray event in a compact region of $\lesssim 20\,r_{\rm g}$ (neither obvious structural changes nor associated flux changes; Akiyama et al. 2015). Such observational evidence may also support the shock-in-jet scenario associated with a VHE event in M87, as some counterpart is reproduced

in our GRMHD simulations. We thus suggest that different behaviors of VLBI cores at different frequencies (43/86 GHz and 230 GHz) can originate from the lateral extent of their sizes ($R/r_{\rm g} \gtrsim 10$ or small), which specifies the location of an emerging high-Γ blob in the PFD funnel jet.

It would be favored to conduct simultaneous observations with multi-frequency, multi-epoch mm/sub-mm VLBI study. This enables us to examine the dynamical structure of the innermost jet in M87 as well as proper motions by diagnosing the core size and the flux variations. For example, an emergence of the blob with $\Gamma \sim 1.5$ near the VLBI core at 86 GHz, as is shown in Figure 19, corresponds to an apparent speed of ~ 0.6–$0.7\ c$ with $\theta_{\rm v} = 14^\circ$. This is equivalent to a motion of ~ 2.2–2.6 mas yr^{-1} in the proximity to M87. By considering the distance between VLBI cores at 86 GHz and 43 GHz as $\sim 20\, r_{\rm g} \sim 0.02$ mas in projection ($\theta_{\rm v} = 14^\circ$), a delay of ~ 2 days is expected before rising the flux density in the VLBI core at 43 GHz, if a passing blob through VLBI cores indeed does cause flare-ups.

5.3.3. *Comparisons with Other Models and Future Studies*

Based on our examination, we briefly discuss other studies on modeling the M87 jet. A "state-of-art" 3D GRMHD simulation model with radiative transfer (RT) computations is proposed by Mościbrodzka et al. (2016a). The model considers that the radio emission comes from the jet sheath (funnel wall:e.g. Hawley & Krolik 2006), in which the plasma is constantly supplied from a less magnetized ($\beta_{\rm p} = 1$–50) accretion disk (e.g. Mościbrodzka et al. 2016b). On the other hand, this paper suggests the jet sheath is powered by the spinning black hole and located inside the parabolic funnel where a highly magnetized plasma exists ($b^2/\rho \gtrsim 1$ and $\beta_{\rm p} \lesssim 1$). Our GRMHD simulations exhibit the bulk acceleration and the superluminal blobs are activated inside, but near the funnel edge at $\gtrsim 10\, r_{\rm g}$ if the black hole spin is moderately large ($a \geq 0.7$; see Figure 19). We therefore suggest that a proper shape of the funnel play an important role in modeling the M87 jet because it may provide a suitable jet sheath if the Doppler beaming and non-thermal particle acceleration by the emerging superluminal blobs are responsible for the limb-brightened feature. As is also discussed in Section 5.3, we remark a highly magnetically dominated state of the VLBA core at 43 GHz (Kino et al. 2014) and the EHT core at 230 GHz (Kino et al. 2015), which may provide an additional constraint on these models. We leave our direct comparison in the forthcoming paper with a post-processing with RT computations.

Mertens et al. (2016) examine kinematics of the M87 jet on scales of $z/r_{\rm g} = 200$–2000 based on multi-epoch VLBA observations at 43 GHz and discuss the jet acceleration[10] in the context of an MHD jet launched by magneto-centrifugal mechanism from the Keplerian disk (BP82). It is unclear whether the BP process indeed takes place at the inner accretion flow near the ergosphere based on our GRMHD simulations (the BP process requires a high magnetization $b^2/\rho \gg 1$ at the jet launching region of the accretion flow and an existence of the coherent poloidal magnetic field, which possibly penetrates the equatorial plane). Authors consider an invisible/dimmer faster spine (than the slower sheath) due to either not present in the flow (i.e., a lower synchrotron particle energy density) or de-boosted. However, as we examined in §5.2, such a de-beaming effect may not be expected on that spacial scale ($z/r_{\rm g} \simeq 1000$) with $\theta_{\rm v} \sim 10^\circ$–$20^\circ$ (e.g. Hada et al. 2016) even if the FFE jet model (an upper limit in the MHD acceleration as the plasma inertia is negligible) is adopted (unless a lower emissivity is expected).

Above two models seem to favor the accretion disk as the origin of the jet sheath, which is contrary to our model. It may be also true that a large-scale coherent poloidal magnetic flux, which threads the equatorial plane, exist in the MAD-type accretion flow (e.g. Tchekhovskoy et al. 2011; Tchekhovskoy & McKinney 2012). We, however, speculate that a highly magnetized (i.e., a low mass loaded, relativistic) outflow may not be initiated in such an environment. It is therefore necessary to examine our hypothesis whether the jet sheath is surely originated from the spinning black hole or not with a MAD-type configuration. Because of how we thread the initial torus with magnetic field, larger disks will have more available magnetic flux to accrete (e.g. Narayan et al. 2012). More accreted flux will then open the possibility of exploring how the MAD state may affect the jet model we propose here. We leave this exploration to future work.

Our results also need to be confirmed in 3D simulations. As observations indicate, projected VLBI images of the M87 jet on the plane of the sky exhibit an almost axisymmetric shape inside the Bondi radius although some internal (non-) axisymmetric patterns exist. This may suggest that internal modes ($m \geq 0$) of plasma instabilities are growing, while external non-axisymmetric modes ($m \geq 1$) seem to be suppressed. This could be the case if the highly magnetized jet is confined by the weakly magnetized external medium (e.g. Nakamura et al. 2007). 3D GRMHD simulation model of M87 (e.g. Mościbrodzka et al. 2016a) exhibits a non-disturbed jet, which may not be subject to external non-axisymmetric modes, at distance up to a few hundred of $r_{\rm g}$.

Finally, we remark on the recent theoretical examination of the limb-brightened jet feature by Takahashi et al. (2018). Based on a steady axisymmetric jet model from the Keplerian accretion disk to synthesize radio images of the M87 jet (Broderick & Loeb 2009), authors examine larger parameter spaces of locating a plasma loading and the angular frequency Ω of the poloidal magnetic field lines. They find that symmetrically limb-brightened jet images as is seen in M87 can be reproduced only if the poloidal magnetic field lines of the jet penetrate a fast-spinning black hole, while the jet with poloidal magnetic field lines that pass through a slowly spinning black hole or the Keplerian accretion disk (at $R/r_{\rm g} \gtrsim 10$), seems to be disfavored[11].

6. CONCLUSIONS

Our study deals with the formation of parabolic jets from the spinning black hole by utilizing semi-analytical solutions of the steady axisymmetric FFE jet model (Narayan et al. 2007; Tchekhovskoy et al. 2008) and the 2D public version of the GRMHD simulation code HARM (Gammie et al. 2003; Noble et al. 2006). Funnel jets in GRMHD simulations, which have been widely investigated during the last decade (see Section 1 for references), are of our particular interest because their nature in a parabolic shape have still been

[10] Authors conduct the wavelet-based image segmentation and evaluation method to derive proper motions. A wider variety of velocity fields is extracted, but the fastest motions at each axial distance are selected to examine the jet acceleration.

[11] The model does not rule out the possibility of a systematic limb-brightened jet if disk-threading poloidal magnetic field lines are spinning fast and concentrated around the ISCO under the high magnetization $b^2/\rho \gg 1$ (e.g. Toma & Takahara 2014).

unknown. Our recent observational efforts toward M87 (see Section 1 for references) provide a case study on this context. We examined funnel jets, especially for their shape, physical conditions at the boundary, and their dependence on the black hole spin, by following McKinney & Narayan (2007a,b) that provided quantitative agreements of the funnel jet interior between the GRMHD simulations and (GR)FFE solutions. We conducted extensive runs up to $r_{\rm out}/r_{\rm g} = 100$ with various black hole spins $a = 0.5$-0.99. Our results highlight a formation of quasi-steady funnel jets in the less-collimated parabolic shape (than the genuine parabolic one: $z \propto R^2$), which does not depend on the black hole spin.

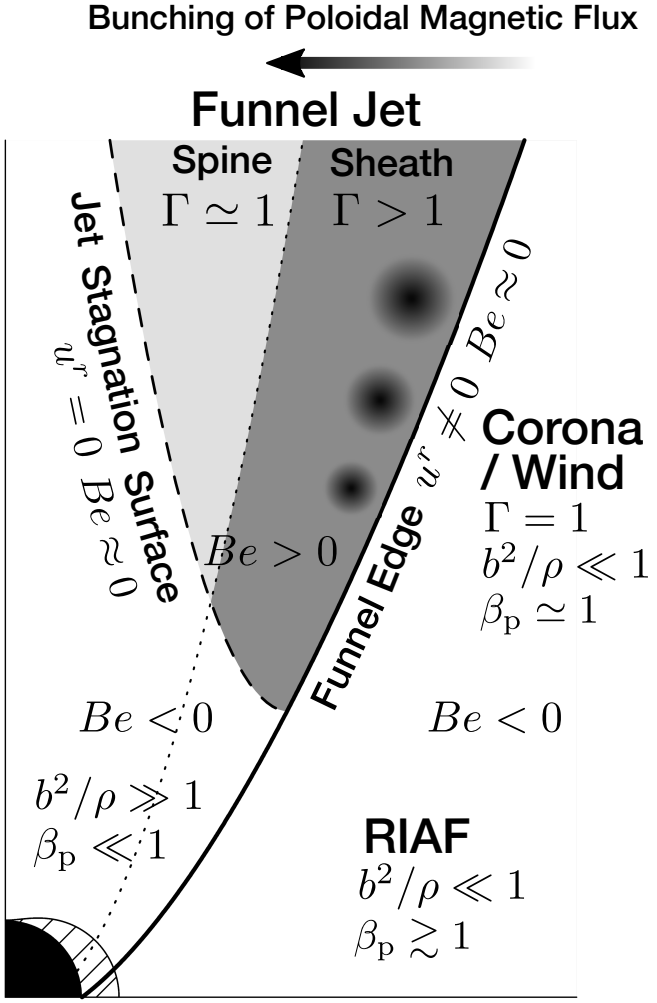

FIG. 20.— Schematic view (arbitrary scale) of our parabolic GRMHD jet with a moderately high spin ($a \geq 0.7$). The system is organized by the highly magnetized funnel (parabolic jet) and the weakly magnetized coronal/wind above the RIAF body. Typical values of the ratio of magnetic to rest-mass energy: b^2/ρ, the plasma-β: $\beta_{\rm p}$, and the Bernoulli parameter: $Be\,(\approx -u_t - 1)$ are specified. The limb-brightened (i.e., spine-sheath) structure is expressed as a context of the lateral stratification of the bulk Lorentz factor: Γ (dark shaded area: $\Gamma > 1$ and light shaded area: $\Gamma \simeq 1$, respectively). The funnel edge ($b^2/\rho \simeq 1$, $\beta_{\rm p} \simeq 1$, $Be \approx 0$, $u^r \neq 0$) and the jet stagnation surface ($Be \approx 0$, $u^r = 0$) are shown as the thick solid and dashed lines, respectively. Emerging blobs are illustrated near the funnel edge.

Schematic view of our parabolic GRMHD jet model is displayed for a moderately high spin ($a \geq 0.7$) in Figure 20. The funnel jet area is highly magnetized (PFD: $b^2/\rho \gg 1$, $\beta_{\rm p} \ll 1$), while the outer area is weakly magnetized ($b^2/\rho \ll 1$) that consists of the RIAF body ($\beta_{\rm p} \gtrsim 1$) and corona/wind ($\beta_{\rm p} \simeq 1$). The funnel edge is approximately determined by the outermost BP82-type parabolic ($z \propto r^{1.6}$) streamline (the ordered, large-scale poloidal magnetic field line) of the FFE solution, which is anchored to the event horizon with an almost maximum angle $\theta_{\rm fp} \simeq \pi/2$ (a thick solid curve in Figure 20), with the following equipartition of i) the magnetic and rest-mass energy densities ($b^2/\rho \simeq 1$) and ii) the gas and magnetic pressures in the fluid frame ($\beta_{\rm p} \simeq 1$). The distribution of $Be \approx 0$ forms a V-shaped geometry in the PFD funnel jet; $Be \approx 0$ is sustained at the funnel edge along the outermost BP82-type parabolic streamline, while the jet stagnation (inflow/outflow separation) surface ($u^r = 0$: a dashed curve in Figure 20) inside the funnel, the location of which depends on the black hole spin (shifting inward with increasing a) (Takahashi et al. 1990; Pu et al. 2015), approximately coincides with the bound/unbound separation: $Be \lessgtr 0$. Note that $u^r \neq 0$ is confirmed at the funnel edge.

At the funnel exterior ($Be < 0$), the coronal wind carries a substantial mass flux (1–3 orders magnitude higher than the funnel jet: cf. Sadowski et al. 2013; Yuan et al. 2015). The magneto-centrifugal mechanism (BP82) would be unlikely to be operated; it is because of the absence of a coherent poloidal magnetic field outside the PFD funnel jet, where the toroidal magnetic field is dominant in the SANE state (see also Hirose et al. 2004, for 3D simulations) and the plasma is not highly magnetized ($b^2/\rho \ll 1$, $\beta_{\rm p} \simeq 1$). Thus, a process of the relativistic MHD acceleration might not be activated (see Equation 1) so that $\Gamma = 1$ is sustained for all cases with $a = 0.5$–0.99 (see also Yuan et al. 2015, with $a = 0$). Note that the situation seems to be unchanged even in the MAD state as is shown in 3D simulations (e.g. Penna et al. 2013, with $a = 0$–0.9).

On the other hand, external environments (corona/wind and RIAF) provide a sufficient pressure support for deforming the funnel jet into a parabolic shape (see also Globus & Levinson 2016); the total (gas + magnetic) pressure (i.e., $\beta_{\rm p} \simeq 1$) is dominant in the corona/wind region, whereas, the ram pressure of the accreting gas near the black hole ($r/r_{\rm g} \lesssim 10$) is the primal component rather than the total pressure of the RIAF body ($\beta_{\rm p} \gtrsim 1$) even in the SANE state. Thus, the latter may conceptually similar to the MAD scenario (Narayan et al. 2003; Igumenshchev 2008; Tchekhovskoy et al. 2011) although the SANE accretion flow does not possess an arrested poloidal magnetic flux on the equatorial plane at $R > r_{\rm H}$.

There is a lateral stratification of Γ in the funnel outflow as a consequence of the unique distribution of b^2/ρ along the jet stagnation surface (a weak dependence on the colatitude angle θ at a few $\lesssim r/r_{\rm g} \lesssim 20$) and the efficiency of the magnetic nozzle effect (see Section 1 for references). The poloidal magnetic flux is differentially bunched towards the central axis by the hoop stress, causing that the magnetic nozzle effect predominantly works at the outer layer in the funnel (sheath: $\Gamma > 1$), while it does not work efficiently at the inner layer of the funnel (spine: $\Gamma \simeq 1$). This is rather general feature in MHD jets from the rotating black hole (e.g. Komissarov et al. 2007, 2009; Tchekhovskoy et al. 2008, 2009, 2010; Penna et al. 2013). Thus, the spine-sheath structure can be naturally expected in MHD jets, being responsible for the limb-brightened feature in AGN jets if the Doppler beaming plays a role (see Figure 20).

An accurate border between the inner jet spine ($\Gamma \simeq 1$) and outer jet sheath ($\Gamma > 1$) is still undefined in our simulations up to $r_{\rm out}/r_{\rm g} = 100$ (though a conceptual border is

drawn in Figure 20), but we would tentatively favor to propose the genuine parabolic inner streamline (BZ77: $z \propto R^2$). Our preceding study (Algaba et al. 2017) gives an additional support; jet radii estimated with VLBI cores for blazars are wider than those of BZ77-type genuine parabolic streamlines ($a = 0.5$–0.998) on $z/r_{\rm g} \simeq 10^4$–10^7. This is rather surprising if we consider the classical scenario (e.g. Ghisellini et al. 2005; Clausen-Brown et al. 2013). A departure from $\Gamma = 1$ may *not* be expected at the funnel edge as far as $b^2/\rho \simeq 1$ is sustained. Therefore, a peak of Γ would be located at some inner layer of the jet sheath. Further numerical study with $r_{\rm out}/r_{\rm g} \geq 10^3$ will be presented in a forthcoming paper.

Based on above results, we apply BP82-type outermost parabolic streamlines of the FFE solution ($a = 0.5$–0.99) to the radius of the jet sheath in M87 derived in multi-frequency VLBI observations. A quantitative agreement (between the FFE solution and VLBI observations) is obtained on the scale of $z/r_{\rm g} \simeq 10$–4×10^5. Same examination is applied to another nearby radio galaxy NGC 6251 on the scale of $z/r_{\rm g} \simeq 10^4$–10^6; we also obtain a similar consistency between the theory and observation (Tseng et al. 2016). Furthermore, a jet structural transition (from parabolic to conical stream) seems to be taken place at around the SOI (Asada & Nakamura 2012; Tseng et al. 2016), suggesting a characteristic of AGN jets, at least in nearby radio galaxies, but possibly even in distant blazars (e.g. Algaba et al. 2017).

We consider limb-brightened features in M87 as a consequence of the bulk acceleration of MHD jets driven by the spinning black hole. The jet sheath, which is organized by an expanding layer between the genuine parabolic (BZ77-type: $z \propto R^2$) and less-collimated parabolic streamlines (BP82-type: $z \propto R^{1.6}$), may be responsible for the Doppler boosted emission toward us with a viewing angle $\theta_{\rm v} = 14°$. Our simulations also exhibit that an emergence of the blob-like knotty feature in the underlying bulk flow (Figure 20). A blob is presumably triggered by the $m = 0$ mode (pressure driven interchange and/or current-driven sausage/pinch) distortion at the funnel edge ($b^2/\rho \simeq 1,\ \beta_{\rm p} \simeq 1$). We propose that it will evolve as a superluminal knot ; axisymmetric knotty patterns are frequently identified in mm/cm VLBI observations (e.g. Niinuma et al. 2014; Hada et al. 2016; Walker et al. 2018).

There is a wider range (more than two orders of magnitude in units of $\Gamma\beta$) of observed proper motions ($\beta_{\rm app} \lesssim 3$) of the jet sheath in M87 at $z/r_{\rm g} \simeq 10^3$–10^4 (Kellermann et al. 2004; Kovalev et al. 2007; Hada et al. 2016, 2017; Mertens et al. 2016). Velocity range fairly matches motions of knotty structures in our simulations (at $z/r_{\rm g} \sim 100$). Therefore, we may expect a blob could be steepen into a shock; one of the possible origins of the shock-in-jet phenomena is reproduced. We expect further detailed examination by utilizing a joint analysis of the VLBI core variability with the EHT, GMVA, HSA, VLBA, and KaVA in order to confirm our hypothesis of the moving shock in the jet. At the same time, as our examination of the beaming factor suggests, much faster motions ($\beta_{\rm app} \approx 4$–$8$ with $\theta_{\rm v} = 14°$) can be expected in the jet sheath at $z/r_{\rm g} \simeq 10^3$–10^4 if the underlying flow follows the highly magenetized MHD/FFE jet evolution. Therefore, one of the challenges for exploring the main stream of the jet sheath would be to conduct a high-cadence VLBI monitoring less than a week (for a faster motion $\gtrsim 0.3$ mas/week).

Our parabolic jet model can be primarily applicable to LLAGNs and/or BL Lacs, in which the RIAF at sub-Eddington regime $\dot{m} \lesssim 10^{-2}$ falls into the central SMBH (Narayan & McClintock 2008). We, however, suggest that the internal structure of a magnetically driven funnel jet ($b^2/\rho \gg 1$ and $\beta_{\rm p} \ll 1$) seems to be general. It would also be expected even in radio loud quasars at a (super-)Eddington regime (no matter how large/small the radiative efficiency is in the accretion flow, a geometrically thick disk accretion plays a role in driving a jet; Tchekhovskoy 2015). Therefore, a faster jet sheath may be universal if the MHD acceleration and collimation play a fundamental role in AGN jets (see also Algaba et al. 2017, for some hints of wider jet radii than $z \propto R^2$ in blazars). As an immediate task, our model needs to be examined with other sources exhibiting limb-brightened structures even with a low viewing angle such as blazars Mrk 421 (Giroletti et al. 2006; Piner et al. 2010) and Mrk 501 (Giroletti et al. 2004, 2008; Piner et al. 2009; Koyama et al. 2016).

M.N. acknowledges Roger Blandford for careful reading of the manuscript and helpful comments. M.N. also thanks Ruben Krasnopolsky for his help with the Python programming. Instructive comments by the anonymous referee helped us to improve the manuscript. TIARA summer school on numerical astrophysics 2015 at ASIAA provided a tutorial for the HARM code. K. Aasada is supported by the Ministry of Science and Technology of Taiwan grants MOST 106-2119-M-001-027 and MOST107-2119-M-001-017. K. Hada was supported by JSPS Grant Number 18K13592 and the Sumitomo Foundation Grant for Basic Science Research Projects Grant Number 170201. K. Toma acknowledges JSPS Grants-in-Aid for Scientific Research 15H05437 and JST grant Building of Consortia for the Development of Human Resources in Science and Technology. This work is partially supported by JSPS KAKENHI grants No. JP18K03656 (M. Kino) and JP18H03721 (K. Niinuma, M. Kino, and K. Hada). J.-C. Algaba acknowledges support from the National Research Foundation of Korea (NRF) via grant NRF-2015R1D1A1A01056807. K. Akiyama is financially supported by the Jansky Fellowship of the National Radio Astronomy Observatory (NRAO) and a grant from the National Science Foundation (NSF; AST-1614868). The NRAO is a facility of the NSF operated under cooperative agreement by Associated Universities, Inc.

REFERENCES

Abramowicz, M. A., Jaroszyński, & Sikora, M. 1978, A&A, 63, 221
Abramowski, A., Acero, F., Aharonian, F., et al. 2012, ApJ, 746, 151
Acciari, V. A., Aliu, E., Arlen, T., et al. 2009, Science, 325, 444
Akiyama, K., Lu, R.-S., Fish, V. L., et al. 2015, ApJ, 807, 150
Algaba, J.-C., Nakamura, M., Asada, K., & Lee, S.-S. 2017, ApJ, 823, 86
Asada, K., & Nakamura, M. 2012, ApJ, 745, L28 (AN12)
Asada, K., Nakamura, M., Doi, A., et al. 2014, ApJ, 781, L2
Asada, K., Nakamura, M., & Pu, H.-Y. 2016, ApJ, 833, 56
Balbus, S. A., & Hawley, J. F. 1991, ApJ, 376, 214
Beckwith, K., Hawley, J. F., & Krolik, J. H. 2008, ApJ, 678, 1180
Beckwith, K., Hawley, J. F., & Krolik, J. H. 2009, ApJ, 707, 428
Begelman, M. C., & Li, Z.-Y. 1994, ApJ, 426, 269
Beskin, V. S., & Nokhrina, E. E. 2006, MNRAS, 367, 375
Beskin, V. S., & Nokhrina, E. E. 2009, MNRAS, 397, 1486
Beskin, V. S. 2010, *MHD Flows in Compact Astrophysical Objects: Accretion, Winds and Jets (Berlin, Heidelberg: Springer)*
Biretta, J. A., Zhou, F., & Owen, F. N. 1995, ApJ, 447, 582
Biretta, J. A., Sparks, W. B., & Macchetto, F. 1999, ApJ, 520, 621
Blakeslee, J. P., Jordán, A., Mei, S., et al. 2009, ApJ, 694, 556
Blandford, R. D., & Königl, A. 1979, ApJ, 232, 34
Blandford, R. D., & Payne, D. G. 1982, MNRAS, 199, 883 (BP82)
Blandford, R. D., & Znajek, R. L. 1977, MNRAS, 179, 433 (BZ77)

Blandford, R. D., & Begelman, M. C. 1999, MNRAS, 303, L1
Blandford, R. D., & Begelman, M. C. 2004, MNRAS, 349, 68
Broderick, A. E., & Loeb, A. 2009, ApJ, 697, 1164
Broderick, A. E., & Tchekhovskoy, A. 2015, ApJ, 809, 97
Camenzind, M. 1987, A&A, 184, 341
Chan, C.-K., Psaltis, D., & äzel, F. 2013, ApJ, 777, 13
Cheung, C. C., Harris, D. E., & Stawarz, Ł. 2007, ApJ, 663, L65
Clarke, D. A., Norman, M. L., & Burns, J. O. 1986, ApJ, 311, L67
Clausen-Brown, E., Savolainen, T., Pushkarev, A. B., et al. 2013, A&A, 558, A144
Contopoulos, J. 1995, ApJ, 446, 67
Cowling, T. G. 1934, MNRAS, 94,768
Dermer, C. D. 2007, ApJ, 659, 958
De Villiers, J.-P., Hawley, J. F., & Krolik, J. H. 2003, ApJ, 599, 1238
De Villiers, J.-P., Hawley, J. F., Krolik, J. H., & Hirose, S. 2005, ApJ, 620, 878
Dexter, J., McKinney, J. C., & Agol, E. 2012, MNRAS, 421, 1517
Doeleman, S. S., et al. 2012, Science, 338, 355
Fendt, C., & Ouyed, R. 2004, 608, 378
Ferraro, V. C. A. 1937, MNRAS, 97, 458
Fishbone, L. G., & Moncrief, V. 1976, ApJ, 207, 962
Gammie, C. F., McKinney, J. C., & Tóth, G. 2003, ApJ, 589, 444
Gammie, C. F., Shapiro, S. L., & McKinney, J. C. 2004, ApJ, 602, 312
Gebhardt, G., & Thomas, J. 2009, ApJ, 700, 1690
Gebhardt, K., Adams, J., Richstone, D., et al. 2011, ApJ, 729, 119
Ghisellini, G., Tavecchio, F., & Chiaberge, M. A&A, 432, 401
Ghisellini, G., Tavecchio, F., Maraschi, L., et al. 2014, Nature, 515, 376
Giroletti, M., Giovannini, G., Feretti, L. et al. 2004, ApJ, 600, 127
Giroletti, M., Giovannini, G., Taylor, G. B., & Falomo, R. 2006, ApJ, 646, 801
Giroletti, M., Giovannini, G., Cotton, W. D., et al. 2008, A&A, 488, 905
Giroletti, M., Hada, K., Giovannini, G., et al. 2012, A&A, 538, L10
Globus, N., & Levinson, A. 2013, Phys. Rev. D, 88, 084046
Globus, N., & Levinson, A. 2016, MNRAS, 461, 2605
Gracia, J., Vlahakis, N., Agudo, I., et al. 2009, ApJ, 695, 503
Hada, K., et al. 2011, Nature, 477, 185
Hada, K., et al. 2012, ApJ, 760, 52
Hada, K., Kino, M., Doi, A., et al. 2013, ApJ, 775, 70
Hada, K., Giroletti, M., Kino, M., et al. 2014, ApJ, 788, 165
Hada, K., Kino, M., Doi, A., et al. 2016, ApJ, 817, 131
Hada, D. 2017, Galaxies, 5, 2
Hada, K., Park, J. H., Kino, M., et al. 2017, PASJ, 69, 71
Harris, D. E., Cheung, C. C., Stawarz, Ł, et al. 2009, ApJ, 699, 305
Hawley, J. F., & Krolik, J. H. 2006, ApJ, 641, 103
Hirose, S., Krolik, J. H., De Villiers, J.-P., & Hawley, J. F. 2004, ApJ, 606, 1083
Igumenshchev, I. V. 2008, ApJ, 677, 317
Jorstad, S. G., Marscher, A. P., Lister, M. L., et al. 2005, AJ, 130, 1418
Junor, W., Biretta, J. A., & Livio, M. 1999, Nature, 401, 891
Kadomtsev, B. B. 1966, RvPP, 2, 153
Kellermann, K. I., et al. 2004, ApJ, 539, 563
Kino, M., Takahara, F., Hada, K., & Doi, A. 2014, ApJ, 786, 5
Kino, M., Takahara, F., Hada, K., et al. 2015, ApJ, 803, 30
Komissarov, S. S. 2004, MNRAS, 350, 427
Komissarov, S. S. 2005, MNRAS, 359, 801
Komissarov, S. S. & McKinney, J. C. 2007, MNRAS, 377, L49
Komissarov, S. S., Barkov, M. V., Vlahakis, N., & Königl, A. 2007, MNRAS, 380, 51
Komissarov, S. S., Vlahakis, N., Königl, A., Barkov, M. V. 2009, MNRAS, 394, 1182
Komissarov, S. S. 2011, Mem. Soc. Astron. Ital., 82, 95
Kovalev, Y. Y., Lister, M. L., Homan, D. C., & Kellermann, K. I. 2007, ApJ, 668, L27
Koyama, S., Kino, M., Giroletti, M., et al. 2016, A&A, 586, A113
Krolik, J. H., & Hawley, J. F. 2002, ApJ, 573, 754
Kronberg, P. P., Dufton, Q. W., Li, H., & Colgate, S. A. 2001, ApJ, 560, 178
Li, Z.-Y., Chiueh, T., & Begelman, M. C., 1992, ApJ, 394, 459
Lico, R., Giroletti, M., Orienti, M., et al. 2012, A&A, 545, A117
Lister, M., Cohen, M. H., Homan, D. C., et al. 2009, AJ, 138, 1874
Lister, M., et al. 2013, AJ, 146, 120
Lovelace, R. V. E., Wang, J. C. L., & Sulkanen, M. E. 1987, ApJ, 315, 504
Ly, C., Walker, R. C., & Junor, W. 2007, ApJ, 660, 200
Lyubarsky, Y. 2009, ApJ, 698, 1570
Lyubarsky, Y. 2010, MNRAS, 402, 353
Macchetto, F., Marconi, A., Axon, D. J., et al. 1997, ApJ, 489, 579
Mahadevan, R. 1997, 477, 585
Mahadevan, R. & Quataert, E. 1997, 490, 605
Marscher, A. P. 1980, ApJ, 235, 386
Marscher, A. P., & Gear, W. K. 1985, ApJ, 298, 114
Matsushita, K., Belsole, E., Finoguenov, A., & Böhringer, H., 2002, A&A, 386, 77
McKinney, J. C., & Gammie, C. F. 2004, ApJ, 611, 977
McKinney, J. C. 2006, MNRAS, 368, 1561
McKinney, J. C. & Narayan, R. 2007, MNRAS, 375, 513
McKinney, J. C. & Narayan, R. 2007, MNRAS, 375, 531
McKinney, J. C., Tchekhovskoy, A., & Blandford, R. D. 2012, MNRAS, 423, 3083
Meier, D. L., Koide, S., & Uchida, Y. 2001, Science, 291, 84
Meier, D. L. 2012, *Black Hole Astrophysics: The Engine Paradigm* (Springer, Heidelberg)
Mertens, F., Lobanov, A. P., Walker, R. C., Hardee, P. E. 2016, A&A, 595, A54
Meyer, E. T., Sparks, W. B., Biretta, J. A., et al. 2013, ApJ, 774, L21
Mościbrodzka, M., Falcke, H., & Shiokawa, H. 2016, A&A, 586, A38
Mościbrodzka, M., Falcke, H., & Noble, S. 2016, A&A, 596, A13
Nakamura, M., & Meier, D. L. 2004, ApJ, 617, 123
Nakamura, M., Li, H., & Li, S. 2006, ApJ, 652, 1059
Nakamura, M., Li, H., & Li, S. 2007, ApJ, 656, 721
Nakamura, M., Garofalo, D., & Meier, D. L. 2010, ApJ, 721, 1783
Nakamura, M., & Asada, K. 2013, ApJ, 775, 118
Nakamura, M., & Meier, D. L. 2014, ApJ, 785, 152
Narayan, R., Igumenshchev, I. V., & Abramowicz, M. A. 2003, PASJ, 55, L69
Narayan, R., McKinney, J. C., & Farmer, A. J. 2007, MNRAS, 375, 548 (NMF07)
Narayan, R., & McClintock, J. E. 2008, New. Ast. Rev., 51, 733
Narayan, R., Jason, Li, & Tchekhovskoy, A. 2009, ApJ, 697, 1681
Narayan, R., Sadowski, A., Penna, R. F., & Kulkarni, A. K. 2012, MNRAS, 426, 3241
Niinuma, K., Lee, S.-S., Kino, M., et al. 2014, PASJ, 66, 103
Noble, S. C., Gammie, C. F., McKinney, J. C., & Del Zanna, L. 2006, ApJ, 641, 626.
Nokhrina, E. E., Beskin, V. S., Kovalev, Y. Y., & Zheltoukhov, A. A. 2015, MNRAS, 447, 2726
Owen, F. N., Hardee, P. E., & Cornwell, T. J. 1989, ApJ, 340, 698
Penna, R. F., Narayan, R., & Sadowski, A. 2013, MNRAS, 436, 3741
Perlman, E. S., Harris, D. E., Biretta, J. A., Sparks, W. B., & Macchetto, F. D. 2003, ApJ, 599, L65
Piner, B. G., Pant, N., Edwards, P. G., & Wiik, K. 2009, ApJ, 690, L31
Piner, B. G., Pant, N., & Edwards, P. G. 2010, ApJ, 723, 1150
Priest, E. R. 1982, *Solar Magneto-hydrodynamics* (Dordrecht: Reidel)
Pu, H.-Y., Nakamura, M., Hirotani, K., Mizuno, Y., Wu, K, & Asada, K. 2015, ApJ, 801, 56
Pu, H.-Y., Wu, K., Younsi, Z., Asada, K., Mizuno, Y., & Nakamura, M. 2017, ApJ, 845, 160
Rafferty, D., McNamara, B. R., Nulsen, P. E. J., & Wise, M. W. 2006, ApJ, 652, 216
Reid, M. J., Biretta, J. A., Junor, W., et al. ApJ, 336, 112
Ressler, S. M., Tchekhovskoy, A., Quataert, E., & Gammie, C. F. 2017, MNRAS, 467, 3604
Reynolds, C. & Fabian, A. 2008, ApJ, 675, 1048
Sadowski, A., Narayan, R., Penna, R., & Zhu, Y., 2013, MNRAS, 436, 3856
Savolainen, T., et al. . 2010, A&A, 512, A24
Stawarz, Ł., & Ostrowski, M. 2002, ApJ, 578, 763
Takahashi, M., Nitta, S., Tatematsu, Y., & Tomimatsu, A. 1990, ApJ, 363, 206
Takahashi, K., Toma, K., Kino, M., Nakamura, M., & Hada, K. 2018, arXiv:1802.00292
Tchekhovskoy, A., McKinney, J. C., & Narayan, R. 2008, MNRAS, 388, 551 (TMN08)
Tchekhovskoy, A., McKinney, J. C., & Narayan, R. 2009, MNRAS, 699, 1789
Tchekhovskoy, A., Narayan, R., & McKinney, J. C. 2010, ApJ, 711, 50
Tchekhovskoy, A., Narayan, R., & McKinney, J. C. 2011, MNRAS, 418, L79
Tchekhovskoy, A., & McKinney, J. C. 2012, MNRAS, 423, L55
Tchekhovskoy, A. 2015, ASSL, 414, 45
Toma, K., & Takahara, F. 2013, Prog. Theor. Exp. Phys., 083E02
Toma, K., & Takahara, F. 2014, MNRAS, 442, 2855
Tomimatsu, A., & Takahashi, M. 2003, ApJ, 592, 321
Tseng, C.-Y., Asada, K., Nakamura, M., et al. 2016, ApJ, 833, 288
Uchida, Y., & Shibata, K. 1985, PASJ, 37, 515
Vlahakis, N. & Königl, A. 2003a, ApJ, 596, 1080
Vlahakis, N. & Königl, A. 2003b, ApJ, 596, 1104

Walker, R. C., et al. 2018, ApJ, 855, 182
Wald, R. M. 1974, Phys. Rev. D, 10, 1680
Walsh, J. L., Barth, A., Ho, L. C., & Sarzi, M. 2013, ApJ, 770, 86
Wang, C.-C., & Zhou, H.-Y. 2009, MNRAS, 395, 301
Yuan, F., Gan, Z., Narayan, R., et al. 2015, ApJ, 804, 101
Zakamska, N. L., Begelman, M. C., & Blandford, R. D. 2008, ApJ, 679, 990

APPENDIX

A. DEPENDENCE OF THE FUNNEL JET SHAPE ON INITIAL PLASMA-β VALUES (LOWER/HIGHER LIMITS)

This appendix provides the range of validity of parabolic funnel jets by showing results with different parameters. We fix the dimensionless Kerr parameter $a = 0.9$, but changes $\beta_{\rm p0,\,min}$ to 50 or 500; snapshots of physical quantities are shown in Figure 21. Compared with the case of $\beta_{\rm p0,\,min} = 100$, overall structures are unchanged (the funnel edge follows the parabolic outermost streamline $z \propto R^{1.6}$: BP82) when we start with $\beta_{\rm p0,\,min} = 50$. A highly magnetized funnel is formed and $b^2/\rho \simeq 1$ is sustained at the funnel edge. The external corona/wind region is qualitatively identical. Note that simulations with $\beta_{\rm p0,\,min} < 50$ sometimes induce numerical errors around the polar axis due to the extremely high magnetization $b^2/\rho \gg 1$.

On the other hand, the magnetization in the funnel is weaken if we start with $\beta_{\rm p0,\,min} = 500$ and $b^2/\rho \simeq 0.3$ is obtained at the funnel edge. The magnitude of the outgoing radial radial mass flux in the funnel region is almost similar with the case of $\beta_{\rm p0,\,min} = 50/100$, while that in the outer coronal wind area is different; about one order of magnitude smaller in $\beta_{\rm p0,\,min} = 500$ than the case of $\beta_{\rm p0,\,min} = 50/100$. It is notable that a departure of the funnel edge from $z \propto R^{1.6}$ is seen at $r/r_{\rm g} > 40$, following a conical expansion (see the distributions of $Be \approx 0$ and $\beta_{\rm p} = 1$ in bottom panels of Figure 21). The distribution of the Lorentz factor exhibits no feature of the inhomogeneous distribution of Γ (blobs) at the outer layer in the funnel for $\beta_{\rm p0,\,min} = 500$.

Thus, Figure 21 exhibits an example how the parabolic funnel jet deforms into a conical shape ($\beta_{\rm p0,\,min} = 500$). Figure 22 provides further qualitative analysis on this issue. The total pressure balance between the funnel region ($\beta_{\rm p} \ll 1$) and the external corona/wind region ($\beta_{\rm p} \simeq 1$) is sustained in the case of the parabolic funnel ($\beta_{\rm p0,\,min} = 50$; *upper* panel). On the other hand, magnetically dominated (total) pressure in the non-parabolic funnel ($\beta_{\rm p0,\,min} = 500$; *lower panel*) is overpressured (a factor of few) against the external coronal/wind region where $\beta_{\rm p} \simeq 1$ is not hold (the gas pressure dominated). The prescription of a higher value of $\beta_{\rm p} \gtrsim 500$ may not be enough to provide a sufficient total pressure, presumably due to a lack of the magnetic pressure. In summary, we suggest that a moderately magnetized wind/corona ($\beta_{\rm p} \simeq 1$) may play a dynamical role in maintaining the funnel jet into a parabolic shape.

B. TIME EVOLUTION OF THE SANE

Figure 23 provides the time evolution of the mass accretion rate $\dot{M}$, the poloidal magnetic flux Φ threading the black hole horizon, and ϕ, the dimensionless ratio of Φ to $\dot{M}c^2$ for our four systems examined in Section 3.2. Following Narayan et al. (2012), $\dot{M}$ is defined as

$$\dot{M} = 2\pi \int_0^\pi \rho u^r \sqrt{-g} d\theta. \tag{B1}$$

Φ is defined as

$$\Phi = \frac{1}{2}\left(2\pi \int_0^\pi |B^r| \sqrt{-g} d\theta\right). \tag{B2}$$

In addition, the normalized poloidal magnetic flux ϕ is considered as follows;

$$\phi = \frac{\Phi}{\sqrt{\dot{M}}}, \tag{B3}$$

which characterizes the degree of the magnetization of the inner accretion flow (e.g. Tchekhovskoy 2015). We evaluate the above quantities at the horizon $r_{\rm H}$.

There is almost no variation of Φ after $t/t_{\rm g} \simeq 4000$ for all cases. We confirm the values of Φ threading the black hole horizon are quantitatively consistent in between our 2D and 3D runs (Mościbrodzka et al. 2016b) with various BH spins. On the other hand, $\dot{M}$ increases in our moderate spin cases ($a = 0.5$ and 0.7) at $t/t_{\rm g} \gtrsim 4000$, while it remains sustained at lower values with time variations in our high spin cases ($a = 0.9$ and 0.99). We note that qualitatively similar tendency ($\dot{M}$ increases at $t/t_{\rm g} \gtrsim 3000$–4000) is confirmed in 3D runs for wider spin cases ($a = 0.1$–0.98; Mościbrodzka et al. 2016b). As a consequence, ϕ never reaches a level of the MAD state in our 2D runs ($\phi \gtrsim 10$ is confirmed in $a = 0.9$ at $t/t_{\rm g} \gtrsim 4000$).

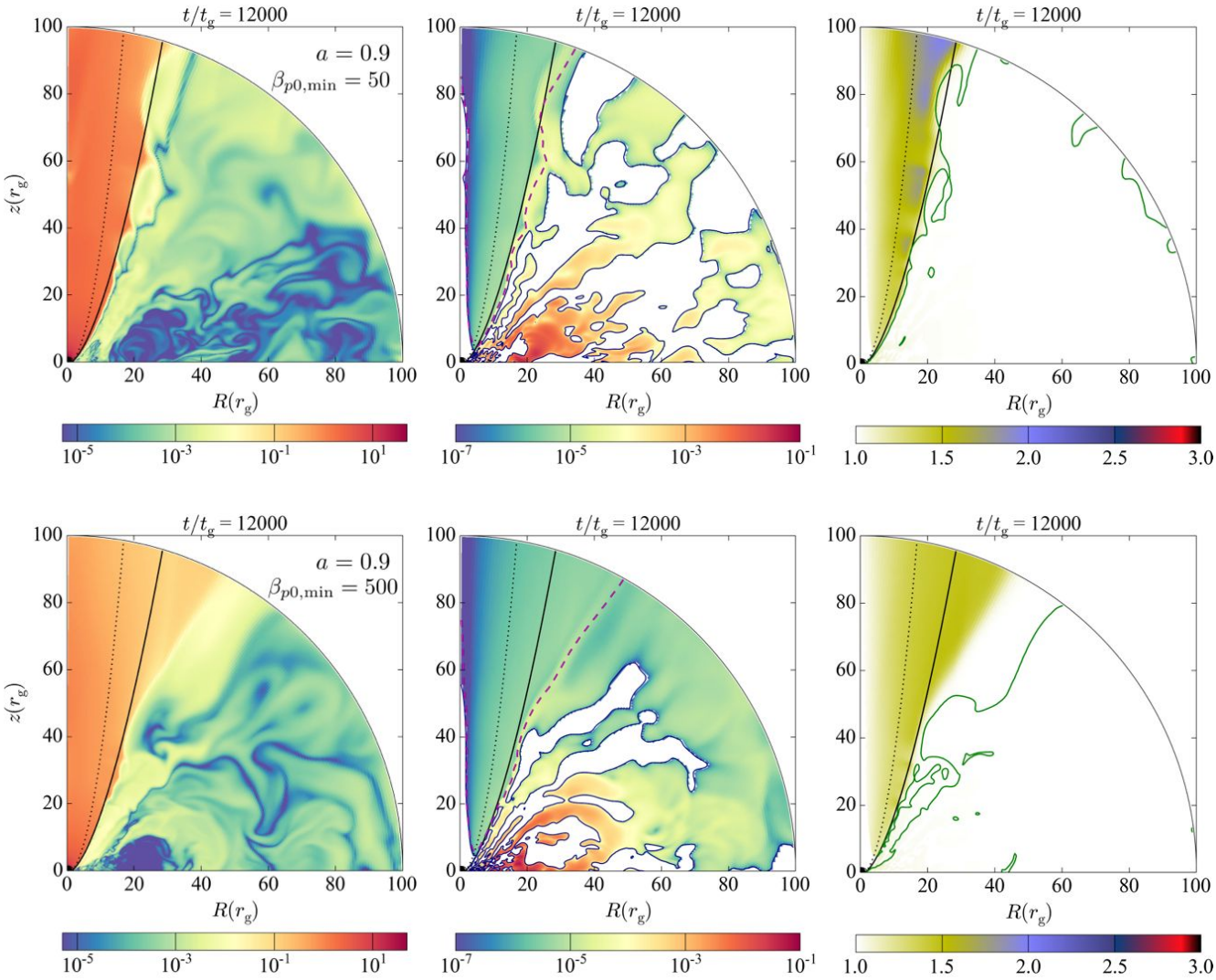

FIG. 21.— Final ($t/t_g = 12000$) snapshots of two different initial conditions (the black hope spin $a = 0.9$ is fixed); $\beta_{p0,\,\min} = 50$ (*top*) and $\beta_{p0,\,\min} = 500$ (*bottom*). A color-filled contour of the magnetic energy per unit particle b^2/ρ (*left*), the magnitude of the outgoing radial mass flux density (*middle*), and the Lorentz factor Γ (*right*). Readers can refer to Figures 8, 11, and 12 ($a = 0.9$) for comparison.

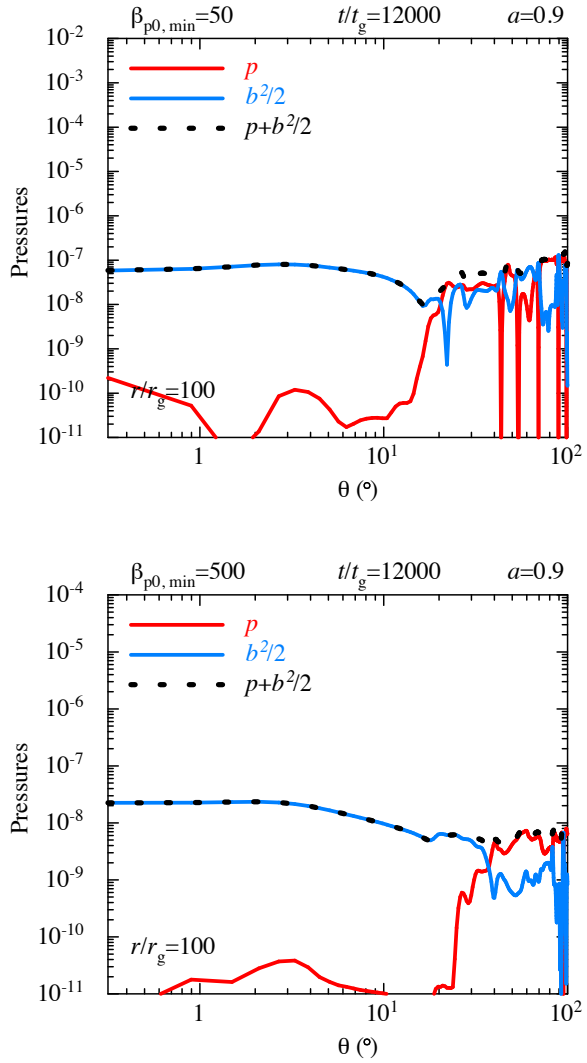

FIG. 22.— A θ cross-section at $r/r_{\rm g} = 100$ showing the gas pressure (red solid line), the magnetic pressure (blue solid line), and their sum (the total pressure: black dotted line) for two different initial conditions ($a = 0.9$ is fixed) at the final stage ($t/t_{\rm g} = 12000$); $\beta_{p0,\rm min} = 50$ (*left*) and $\beta_{p0,\rm min} = 500$ (*right*). Readers can refer to the *top* panel of Figure 10 ($a = 0.9$) for comparison.

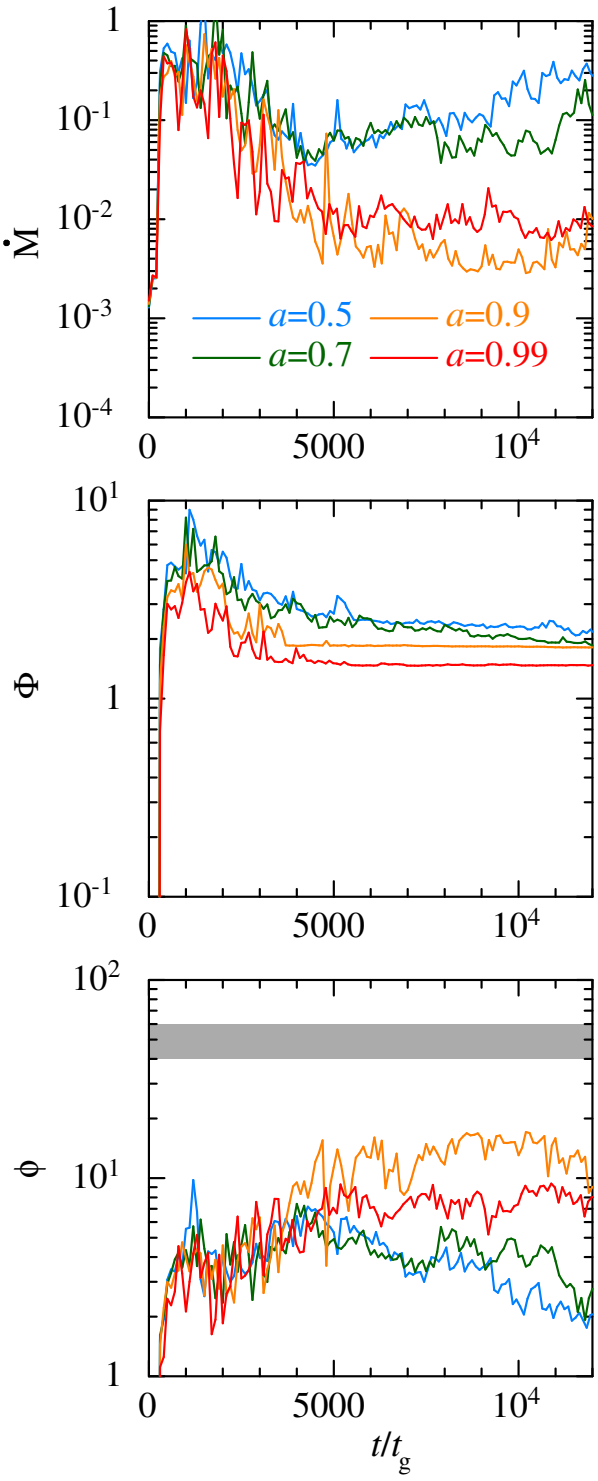

FIG. 23.— Variations of $\dot{M}$ (*top*), Φ (*middle*), and ϕ (*bottom*) as a function of time with varying black hole spin, corresponding to four different cases in Section 3.2. $\phi \approx 40$–60 (MAD state) is indicated as gray shaded area in the *bottom* panel.